CASE STUDY

The retrofitting of ships by applying retractable bow hydrofoils: a case study

Karol Niklas[1] · Hanna Pruszko[1]

Abstract

Increasing environmental requirements and a relatively long ship life of 30 years mean more attention is needed to retrofit existing ships. One possibility is using hydrofoils to reduce the ship's resistance and improve comfort and safety in rough sea conditions. This study investigates the influence of retractable bow hydrofoils on the seakeeping performance and operational conditions of a selected case study vessel (V-shaped bulbous bow). The methods used were full-scale computational fluid dynamics (CFD) simulations and towing tank experiments for validation. The analysis was conducted for bow waves of different lengths and a ship's operating speed. The most beneficial effect of hydrofoils was observed for wavelengths from $\lambda/L_{WL} = 1.0$ to $\lambda/L_{WL} = 1.2$. For the wavelength $\lambda/L_{WL} = 1.2$, the reduction of heave motion was equal to 33%, pitch motion was equivalent to 28%, and the reduction of wave-added resistance was equal to 25%. The analysis also showed unfavourable conditions for which hydrofoil folding is needed to avoid causing an excessive increase in resistance. A generalized procedure has been developed to assess the potential for resistance and motion reduction by retrofitting existing ships using hydrofoils.

Keywords Ship · Seakeeping · Retrofitting · CFD · Hydrofoils

1 Introduction

In recent years, there has been significant interest in raising the propulsive efficiency of ships and improving comfort and safety. This is supported by the rapidly growing requirements for environmental protection. It is worth noting that the working life of a ship is about 30 years. Therefore, to significantly reduce emissions from maritime transport over the next 10–30 years, more attention should be paid to retrofitting the existing fleet. One possibility worthy of attention is using bow hydrofoils (analyzed here) to improve ships' seakeeping performance.

Multiple studies have been carried out to investigate the application of hydrofoils in ships. In the early 1980s, a Norwegian fishing vessel was equipped with two foils on its bow. Additional thrust was produced, and pitching and rolling reduction was observed (Berg 1985). Similar findings were reported by Terao and Isshiki (1991), who carried out tests on a full-scale fishing vessel. Belibassakis and

Politis (2013) analyzed the hydrodynamic performance of a flapping wing beneath the ship's hull. Numerical results presented the thrust the examined biomimetic system produced and the ship's vertical motion reduction. Bøckmann and Steen (2013) analyzed the experimental results with a model with a fixed horizontal hydrofoil attached deep below the bow. The foil resulted in a resistance reduction of up to 60% in regular head sea waves. The potential for extracting a ship's kinetic energy using a biomimetic wing with active pitch control was studied (Politis and Politis 2014). It was concluded that significant propulsion power might be produced, and the stabilizing effect was also noted. Free surface impact on the flapping foil performance was analyzed by Filippas and Belibassakis (2014). Belibassakis and Filippas (2015) analyzed the coupling between ship motions and flapping foil dynamics. Placing the wing on the bow was beneficial regarding thrust generation. Bowker et al. (2015), Bowker (2018) also studied the application of flapping foils. The possibility of using the foils for propulsion and as the device that transfers the wave energy to the power take-off system was analyzed. The flapping foil stabilizers for the S-SWATH vessel were investigated (Wang et al. 2016), and the motion control model, coupled with the mathematical force

✉ Karol Niklas
 karol.niklas@pg.edu.pl

1 Gdansk University of Technology, Narutowicza 11/12,
 80-233 Gdańsk, Poland

model of flapping foils, was presented. Significant improvement was observed in damping the heave and pitch of ship motions in rough seas. The application of hydrofoil on a selected wind farm support vessel was presented by Aktas et al. (2016). CFD simulations have shown power savings of up to 10%. Bøckmann and Steen (2016) analyzed the experimental model with the wave foil attached to the vessel's bow. Depending on wave parameters, resistance reduction varied between 9 and 17%, heave reduction varied between 11 and 32%, and pitch motion varied from 11 to 25%. Sheng-Wei et al. (2016) also analysed an active pitch-oscillating fin. The free-running model showed energy savings of up to 19%. Active flapping foils in deepwater heading waves were analyzed by Xu et al. (2017). The benefits of applying hydrofoils for thrust generation and motion stabilization were also discussed by Ahmed et al. (2017). A biologically inspired hydrofoil plate installed on a catamaran was presented by Yasukawa and Ishikawa (2017). The concept of retractable bow foils was analyzed (Bøckmann et al. 2018). It was found that the application of retractable foils offered 22% of fuel-saving, in the most favorable case. A similar study was presented by Chiu et al. (2018); however, the free-running ship model was equipped with an actively controlled bow foil. (Jiao et al. 2018) investigated the effects of semi-submerged bow and fin on hull vertical motion stabilization for high speed hybrid ships. They also developed improved strip theory seakeeping algorithm, which considers the viscous flow effects attributed to bow appendages. It is worth noting that for the seakeeping analysis, the standard strip theory method may be insufficient (Niklas and Karczewski 2020) and should be complemented by other methods. In particular, the full-scale CFD-RANS method can be used, i.e. (Niklas and Pruszko 2019a) compared two hull forms, (Huang et al. 2021) analyzed ship seakeeping behaviour in the bi-directional cross wave (Niklas and Pruszko 2019b) showed a supporting role for towing tank testing. In Bowker (2018), the dynamics between vessel and foil in waves were studied. The influence of a foil's location and size, favourable hull dimensions, and optimum wavelength for the highest efficiency of propulsion were investigated. The influence of fixed tandem hydrofoils on the motions of catamaran ships in regular head waves and low forward speed was analyzed (Wang et al. 2019). Also, the stern flap effect on a catamaran's seakeeping characteristic was investigated by Wang et al. (2020). A dual-flapping foil system was analyzed using a 2D parametric study by Moreira et al. (2020). The effect of flexibility on the propulsive performance of a heaving hydrofoil was presented by Li et al. (2021). The highest values of propulsive efficiency were indicated for the analyzed conditions. The seakeeping analysis of a small catamaran equipped with hydrofoils was numerically analyzed by Suastika et al. (2021). A major positive effect of the hydrofoils on reducing ship motions was noted. A wave foil with a passive angle of attack was investigated by Zhang et al. (2022). Two wave foils were analyzed deep below the ship's bow and stern-mounted on long arms. The analysis showed that the wave foil can extract wave energy to propel the ship and reduce the pitch motion of the ship. The propulsion and energy harvesting performance of a pitching foil without a hull was investigated by Wang et al. (2022). For specific conditions, high energy harvesting efficiency was obtained. The experimental investigation of the control strategy of a T-foil for increasing the seakeeping performance of a high-speed trimaran was presented by Jiang et al. (2022). The towing tank tests showed that the hybrid control strategy effectively reduced the hull motions. Stark et al. (2022) indicated that the hydrodynamics of the ship's hull could be improved by using different foils in the bow or stern region.

Summarizing the recent studies, improving a ship's seakeeping performance through hydrofoils is an actual research topic being developed in various aspects. At the same time, a relatively small number of papers have examined the most common monohull form, a V-shaped bulbous bow. Difficult operating conditions (North Sea, Baltic Sea), specifically steep waves, are also relatively rarely analyzed. The presented work also uses a foil type with a small aspect ratio and relatively small size, which is much easier and cheaper to implement practically compared to most of the solutions discussed in the literature review. From the perspective of modernizing the existing fleet, this is a significant gap to fill. Also, the capabilities of the Full-scale CFD method have not yet been used to thoroughly analyze the hull-foil interaction with fluid viscosity and free surface effect. Some new aspects are analyzed using the full-scale CFD-RANS method: the time history of thrust and lift force generated by hydrofoils, the time history of bow accelerations, the occurrence of the dynamic stall and the emergence of hydrofoil from the water. It has provided a more detailed insight into the hydrodynamic behaviour of a ship with retractable fixed-angle hydrofoils on the bow.

2 Aim and scope

The study aimed to investigate the influence of retrofitting in the form of retractable fixed-angle bow hydrofoils on the seakeeping performance of a selected case study vessel and its operational conditions. The research demonstrates the potential of retrofitting an existing vessel to reduce the ship's resistance and motions. It was assumed that the hydrofoils can extend and retract in the hull depending on operating conditions, particularly the sea state. A hypothesis is proposed: it is possible to determine the operating conditions for which bow hydrofoils are beneficial by applying full-scale CFD simulations. That is the condition for which simultaneous reductions of total hull resistance, pitch, heave motion,
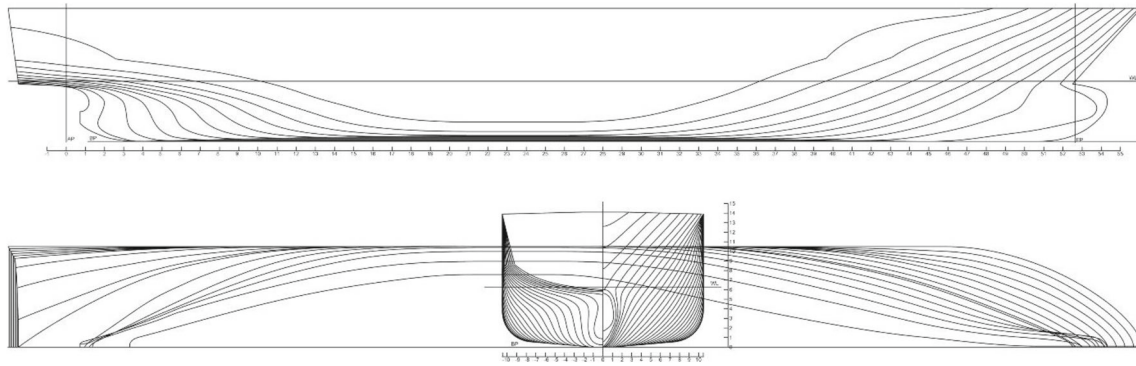
Fig. 1 Body lines of the case study ship

and vertical acceleration are obtained. At the same time, the research is intended to determine conditions under which the presence of hydrofoils is unfavourable. A generalized procedure has been developed to assess the retrofitting of existing ships by adding hydrofoils. The method was successfully applied to the selected vessel.

The scope of the research was as follows. At first, calm water analysis was conducted for a speed range of 5–15 knots. Then, the seakeeping analysis was performed by employing full-scale CFD-RANS simulations for the model with and without the hydrofoils, for the Froude number $F_N = 0.23$, corresponding to the ship's operational speed of 10.4 knots and for a wide range of wavelengths. Furthermore, towing tank tests were performed for the related conditions but with a limited wavelength range to gain validation data. The applied full-scale CFD simulation technique enabled the investigation of the influence of fixed bow hydrofoils on the added wave resistance, heave, pitch, and vertical hull accelerations for selected operational conditions.

3 The case study vessel and the hydrofoils

The research and training vessel 'Nawigator XXI' (IMO 9161247) was chosen. She has a conventional hull form with a V-shaped bow section and flare, a bulbous bow, and a transom stern. The body lines of the ship are presented in Fig. 1. The main operational sites of this ship are the Baltic Sea and the North Sea, characterized by short and steep waves. The ship crew reports that for sea states above 3–4, significant ship motion causes seasickness in people on board. Her real-life seakeeping performance is much worse than expected and calculated using the strip theory method (Niklas and Karczewski 2020). The seakeeping performance determined by full-scale CFD and measured in a towing tank exposed low seaworthiness (Niklas and Pruszko 2019a). Therefore, it is advisable to study the effect of retrofitting in the form of bow hydrofoils on the seakeeping performance. It was determined that the simplest form of hydrofoils was desirable.
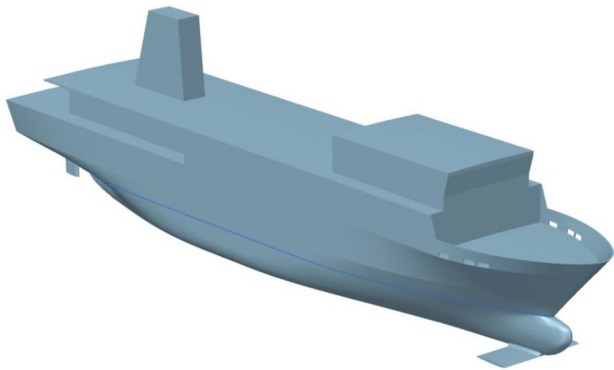
Table 1 Main data of the case study ship

Name	Nawigator XXI
IMO no	9161247
Volume of displacement D (m³)	1110
Waterline length L_{WL} (m)	55.68
Length between perpendiculars L_{pp} (m)	54.13
Breadth B (m)	10.5
Draught $T_{midship}$ (m)	3.14
Longitudinal center of buoyancy L_{CB} (%)	47
Wetted Surface A (m²)	677
Waterplane Area A_{WL} (m²)	466.13
Block coefficient C_B (–)	0.607

Moreover, a fixed angle of attack and the ability to extend and retract into the hull was required (Table 1). According to the wave global statistics, the most frequently occurring weather conditions in the Baltic Sea and the North Sea are waves with a significant height between 1 and 2 m and a zero-crossing period between 4 and 7 s. The corresponding wavelength is between 30 and 70 m. Thus, the wavelength-to-ship length ratio is between $\lambda/L_{WL} = 0.6$ and $\lambda/L_{WL} = 1.3$.

The use of hydrofoils in the analyzed case study vessel reduces vessel motions and added wave resistance. Generating a possible thrust force on the foils is assumed to be less critical. The parameters of hydrofoils, like type, shape, dimension, position, and angle of attack, were selected based on preliminary research and the literature review. The profile selection from the NACA catalogue was dictated by the availability of results describing the hydrodynamic properties of the foils and by meeting the following selection criteria. Firstly, it was to be a symmetric profile because of the symmetric character of oscillatory ship movements. The choice of profile NACA 0010 was based on the desire for low resistance. The span dimension resulted from the practical applicability criteria of the vessel (space available).

Table 2 Main data of the hydrofoil

Profile [–]	NACA0010
Span (tip to root) [m]	3
Chord [m]	2.8
Aspect Ratio AR [–]	1.1
Area A_{FOIL} [m^2]	8.35
Position from FP [m]	0.95
Volume of the hydrofoil [m^3]	1.3

Fig. 2 Model overview of the ship's geometry with the hydrofoils

The chord dimension resulted from the minimum hydrofoil area needed for pitch movement suppression and keeping the aspect ratio above 1. As a result, the foil span was equal to 3 m with an area of 8.35 m^2, which resulted in an aspect ratio of AR = 1.1. The foil chord was equal to 2.8 m with no tapering. The position of the hydrofoil along the ship was dictated by the desire to place it as far as possible towards the ship's bow. This increased the vertical force the arm generated on the foil, suppressing a pitch movement. It was placed 0.95 m behind the fore perpendicular to integrate it into an existing hull form. The total foil area was 16.7 square meters, which gives the ratio between the wing area and the ship waterplane area of 3.6%. In the analyzed case, the hydrofoils have changed the ship's displacement by 0.2%, which has a minor influence on trim and sinkage. The foil data are summarized in Table 2. Overall the hydrofoil type and dimensions can provide relatively easy application in terms of standard materials and low cost. If the budget for a potential retrofit of the vessel allows, a more complex process of selecting the type and dimensions of the hydrofoil with consideration of an optimization process is recommended.

Figure 2 presents the overview model of the case study ship with the hydrofoils.

4 Full-scale CFD simulations

4.1 Numerical model

Simulations were performed using an unsteady RANS approach. The fluid flow was simulated as three-dimensional, viscous, unsteady, and turbulent. The finite volume method was applied to solve the governing equations of mass and momentum conservation, and Star CCM+ software was used. Two different set-ups of numerical simulations were applied: calm water and seakeeping computations. The differences included mesh, temporal discretization, and computational domain size.

In principle, the finite volume method is based on discretizing the entire numerical domain by the computational grid and solving the conservation equation in integral form in each mesh cell of the computational domain. Discretization of the numerical domain means dividing it into a finite number of control volumes. The control volume boundaries define those control volumes (CV). Inside each CV is a computational node. Depending on the problem, the CV can be two- or three-dimensional. The surface and volume integrals must be approximated to obtain the algebraic equation for the particular control volume (Ferziger and Peric 2002). The conservation equation governs each mesh cell's mass, momentum and energy conservation and the entire domain. Moreover, for various problems, the discretization of the conservation equation can be done only in space (steady problems) or space and time (unsteady flow).

The Reynolds-averaged Navier stokes equation is one of the most popular approaches to turbulent model flow next to detached Eddy simulations and large Eddy simulations. It is widely used because of its reasonable computation time and good accuracy. One of the consequences of turbulent flow is the presence of numerous eddies of different scales near the ship's surface. Neither small nor big eddies are directly resolved in the RANS approach, but their average effect on the flow is modelled. The process of averaging causes an additional, previously unknown term—Reynolds stresses—to appear in the equations, written as follows:

$$\frac{\partial(\rho \overline{u_i})}{\partial x_j} = 0, \tag{1}$$

$$\frac{\partial(\rho \overline{u_i})}{\partial t} + \frac{\partial}{\partial x_i}\left(\rho \overline{u_i u_j} + \rho \overline{u'_i u'_j}\right) = \frac{\partial \overline{p}}{\partial x_i} + \frac{\partial \overline{\tau_{ij}}}{\partial x_i}, \tag{2}$$

where p is pressure, ρ is the fluid density, $\rho \overline{u'_i u'_j}$ are Reynolds stresses, u'_i are the averaged components of the velocity vector in the Cartesian system of coordinates, and τ'_{ij} are the

Journal of Ocean Engineering and Marine Energy

Table 3 The set-up of the CFD domain for calm water simulations

Boundary	Position	Boundary Condition
Inlet	2.12 Lpp in front of a ship	Velocity inlet
Outlet	2.2 Lpp behind a ship	Pressure outlet
Symmetry	Symmetry plane of a ship	Symmetry
Side	2.2 Lpp from symmetry plane	Velocity inlet
Top	1.5 Lpp above the free surface	Velocity inlet
Bottom	2.0 Lpp below the free surface	Velocity inlet

mean viscous stress tensor components (defined as follows):

$$\overline{\tau_{ij}} = \mu\left(\frac{\partial \overline{u_i}}{\partial x_j} + \frac{\partial \overline{u_j}}{\partial x_i}\right). \tag{3}$$

The Reynolds stresses tensor needs to be resolved using a turbulence model to close the new system of equations. Over the years, many turbulence models have been defined, and it requires some knowledge and experience from the user to choose and specify them correctly. In this case, the k-ε was selected for the calm water and the seakeeping simulations.

Two degrees of freedom were released—rotations about the Y-axis, resulting in pitching motions, and translations along the Z-axis, resulting in heave motions. The remaining four degrees were restrained. The DFBI (dynamic fluid body interaction) model was applied to compute the ship's motions due to acting fluid forces. The solver allows computation of the motions of a rigid body by integrating pressure and shear forces over the body's surface. The solver iteratively finds a new hull position after the translational motion and angular rotation of a body's center of mass. A surface-capturing VOF (volume of fluid) model was applied to capture the interface between phases. The model can find the actual position of the free surface based on the information on the percentage amount of phases in each cell. The interface is set for cells where the air and water percentage equals 50%. The following sections describe the differences in the numerical settings for simulating the calm water and the seakeeping analyses.

4.1.1 Calm water

For the calm water simulations, a single-volume mesh was applied. The position of outside boundaries of the numerical domain, with prescribed conditions, is described in Table 3. The domain size and ship position were specified to avoid

reflection from the side and downstream boundary and capture the Kelvin wave pattern. Additionally, numerical wave damping was applied to minimize the reflections of waves on the side and outlet boundaries. Standard refinements in the free surface, the wake, and near the hull were used. The numerical model set-up was similar to the one presented, discussed, and analyzed in detail in (Niklas and Pruszko 2019b).

Moreover, because of the presence of hydrofoils, particular surface refinement was applied in the simulations to reproduce the leading and trailing edge of the wing correctly. The prism layers were used in the closest proximity to the hull surface. The value of the non-dimensional distance to the wall y+ was between 50 and 200, which means that the wall function was applied to resolve the boundary layer's velocity profile. The total number of volumetric cells was equal to 2.1 million and 2.6 million for simulations without and with a wave foil. Figure 3 presents the numerical mesh applied for calm water simulations.

A second-order upwind numerical scheme was used for the spatial discretisation convection term, and a first-order scheme was used for temporal discretization. For calm water simulations with a wave foil, the time step varied according to the speed of the vessel to obtain a sufficiently low Courant Number, which is defined as:

$$C = \frac{u\Delta t}{\Delta x}. \tag{4}$$

In this equation, u stands for the fluid velocity, Δt is the time step size, and Δx is the volume element size. This number represents the number of cells fluid particles travel to within one step. It is assumed that it is sufficient for naval applications in calm water simulations to keep the Courant Number below 10.

4.1.2 Regular wave for the seakeeping analysis

The fifth-order Stokes wave model was used to represent the conditions of incoming regular head waves. A probe was placed in front of the bow to monitor the free surface elevation, which enabled control of the actual wave parameters affecting the ship. The overset mesh technique was used because of the expected significant vertical motions of the vessel. This approach is based on the principle that numerical mesh can be divided into two separate regions: the overset and the background region, marked in Fig. 3. The former is placed close to the hull and allowed to translate and rotate freely, according to the computed 6 DOF body motion in the stationary background region. The transport of scalar values between the two areas occurs, which is crucial for the stability of computations and accuracy of the results to ensure that the size of the elements for the two regions is similar at their interface.
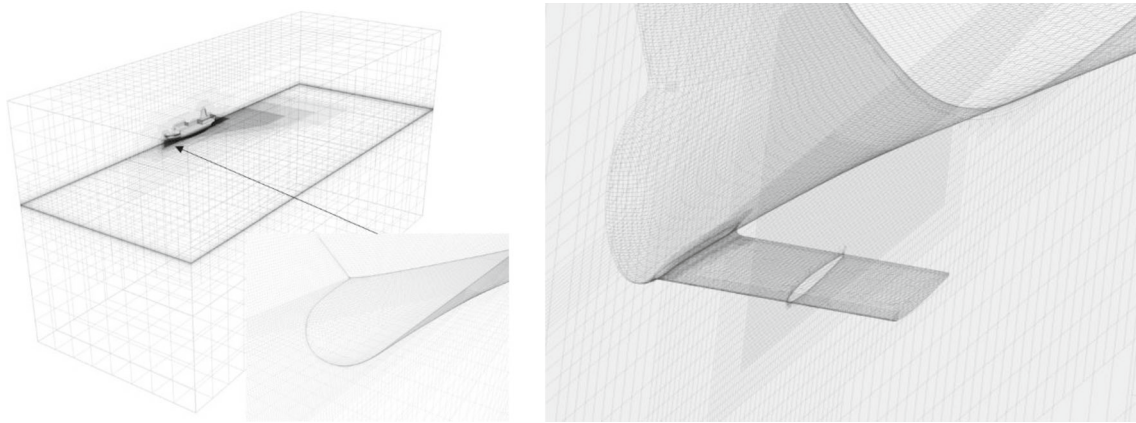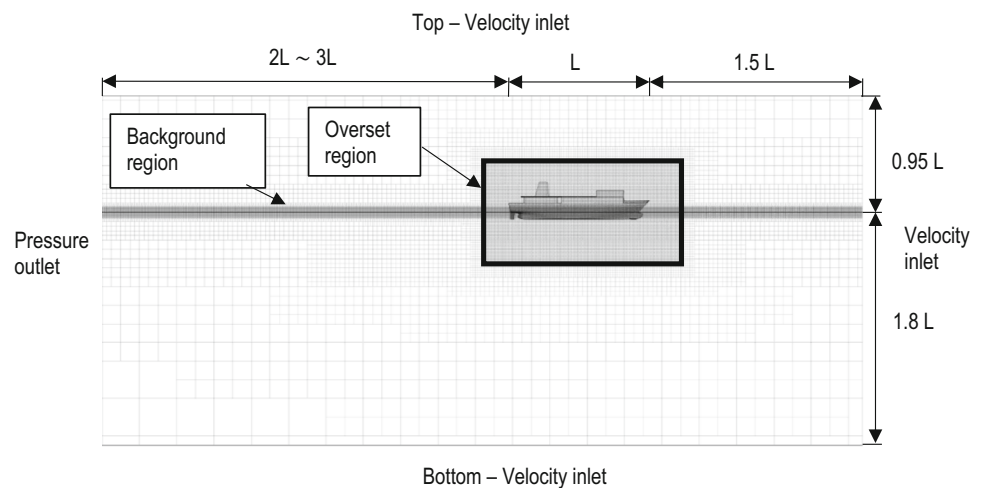
Fig. 3 General view of the finite volume mesh used in the simulation on calm water without the foil (left) and with the refinement of the hydrofoil surfaces (right)

Fig. 4 The finite volume regions and the size of the computational domain used in the seakeeping simulations

Depending on the wavelength, the domain size was more significant for the seakeeping simulations. The upstream inlet boundary was positioned at 1.5 LPP in front of the ship's bow for all the simulations. The top and bottom boundaries were set at a distance of 0.95 L and 1.80 L away from the free water surface, respectively, as shown in Fig. 4. The distance between symmetry, boundary, and side boundary varied between 1.5 L (for short waves) and 2.0 L (for long waves). The distance from the ship and downstream pressure outlet boundary ranged from 2 to 3 L for long waves. The dimensions of the overset region were: 1.13 L long, 1.15 B wide, and 1.6 H high. As specified in Table 3, the velocity inlet conditions were prescribed to the side boundary of the computational domain.

A different modelling approach (from the one applied in the calm water simulations) was used to avoid the undesired reflections from the outlet and side boundaries. The wave force was applied instead of damping. The difference between those approaches is that the free surface elevation next to the boundaries is modified to follow a specified wave profile instead of a flat wave. To select proper forcing coefficients, open-source code was used, according to the detailed description published by Perić and Abdel-Maksoud (2018).

It was noted that the second-order implicit numerical time scheme has very high requirements regarding the time step to ensure the stability of the computations. Based on the authors' experience and previous calculations, it is believed that the biggest challenge is in cases where the ship length is close to the wavelength. To make sure that a less demanding first-order scheme can produce accurate results, the time step dependence study was carried out for the case study ship sailing at a speed of 10.4 knots on a regular head wave of 1.5 m and a period of 6.5 s, which corresponds to $\lambda/L_{WL} = 1.19$. The second-order converged solution required the time step $\Delta t = 0.001$, and it corresponded to 6500-time steps per period of encounter. For the first-order temporal discretization, the time step equal to $\Delta t = 0.0025$ was sufficient for the stability of the computations. The calculated relative difference of pitch, heave, and total resistance allowed us to
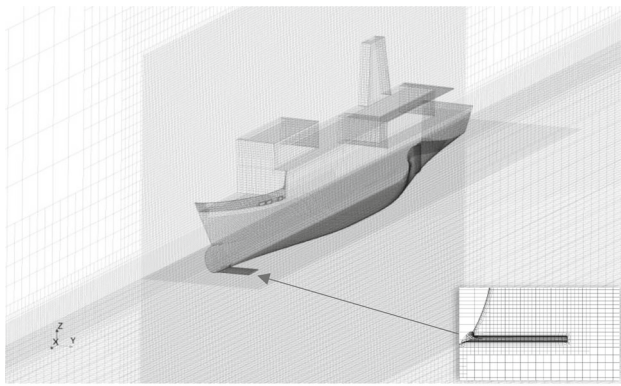
Fig. 5 Mesh refinement of the free water surface at the overset region and the hydrofoil refinement at the FP cross-section

conclude that, despite some damping, this accuracy is acceptable. The differences in the results (namely pitch, heave, and total resistance amplitudes) do not exceed 5%. The numerical mesh and domain used for the seakeeping study were similar to those described in Niklas and Pruszko (2019a). In that paper, the seakeeping performance of the case study vessel was assessed for a regular head wave with a broad range of wavelengths, the wave height equal to 1.95 m and vessel speed Fn = 0.11 and Fn = 0.22. Some of the findings from that investigation were applied in the current study. Special care was taken to refine the mesh properly around the wave foil. In Fig. 4, the transverse cut at the position of the foil is presented with the free surface and the overset region refinement. The total number of elements varied according to the wavelength and was between 4.7 and 7.5 M cells (Fig. 5). The number of cells in the overset region varied between 1.6 and 2.2 M, whereas it was between 3.2 and 5.4 M for the background. The verification study of the numerical model of the vessel without hydrofoils was presented in detail in Niklas and Pruszko (2019a). Therefore, it has not been duplicated here.

However, an additional verification study was conducted for the vessel equipped with hydrofoils. The verification study was performed for three meshes and selected wavelength equal to λ/Lpp = 1.199. A factor systematically reduced the base size of the mesh $\sqrt{2}$ resulting in a total element count equal to 3.5 M, 8.5 M and 20 M of elements for coarse, medium and fine meshes, respectively. Figure 6 shows the results of the verification study.

The verification study was conducted based on the ITTC guidelines (ITTC 2017). The verification analysis indicated that for resistance and motions, monotonic convergence was obtained since the convergence ratio R_G was equal to 0.403, 0.431 and 0.801 for total resistance, pitch amplitude and heave amplitude, respectively. The corrected simulation solution S_C was equal to 83.48 kN for total resistance on waves, 2.25 deg for pitch motion amplitude and 0.384 m for heave

amplitude, giving the mesh uncertainty equal to 2.2% for resistance, 0.9% for pitching motion and 2.5% for heave motion. For further calculations, medium fidelity mesh was chosen to offer a good compromise between accuracy and computation time.

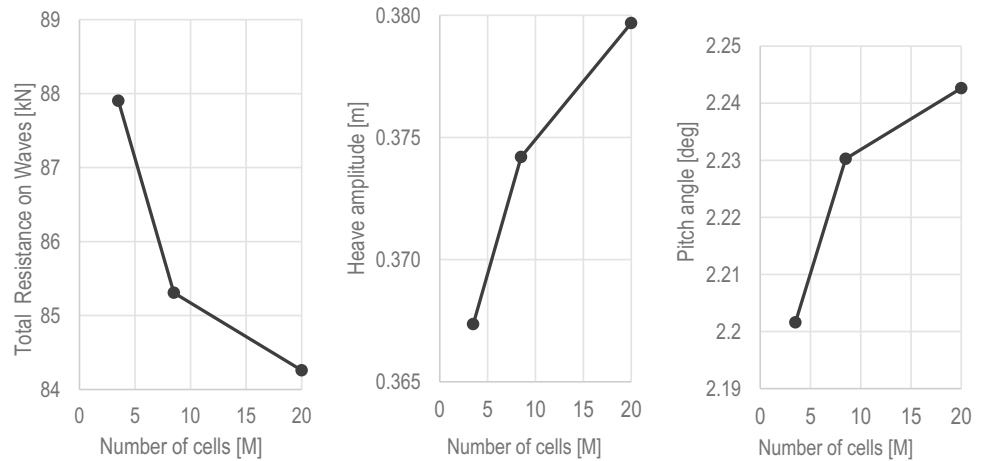## 4.2 Towing tank experiments for validation of the numerical model

The calculations were validated against a towing tank experiment conducted at a 1:25 scale in the Gdansk University of Technology hydrodynamics laboratory. The model basin was 40 m long, 3 m deep, and 4 m wide and equipped with a towing carriage with a maximum speed of 2.5 m/s and a wave generator capable of producing a regular sine wave and irregular wave spectra, including Pierson-Moskovitz, JONSWAP, and ITTC. The towing tank was also equipped with a standard damping beach. The wave probe monitored the wave parameters. The ship model was ballasted according to draft marks, and the moment of inertia was adjusted using a pendulum method. The model was attached to the carriage by a single towing post that allowed it to pitch and heave. The remaining degrees of freedom were restrained. The total resistance, vertical motions, and accelerations at the fore and aft perpendiculars were measured during the run. The data acquisition frequency was equal to 100 Hz. Figure 6 shows the model during testing.

The experimental results presented in this paper consist of four series:

- Series 1—calm water experiment for a ship model as-built.
- Series 2—calm water experiment for a ship model equipped with the wave foil.
- Series 3—seakeeping experiment on the regular head wave for a ship model as-built.
- Series 4—seakeeping experiment on the regular head wave for a ship model equipped with the wave foil.

For calm water in Series 1, the range of speeds for which the model was tested was 0.5 m/s to 1.6 m/s and 0.1 m/s increments. The range of Reynold's Number was between 1.1 $\times 10^6$ and 3.3 10^6, and the trip wire was installed in the fore section of the model to ensure the turbulent flow on the ship's surface. There was no turbulence stimulation on the foil, but the foil was 3-D printed, resulting in an excellent rough surface. The effect of hull roughness was included in the towing tank testing, and the roughness allowance ΔC_F was included. The presented case was calculated based on Bowden–Davison formula. Hull roughness, according to ITTC (2017), was assumed to be $k_S = 150$ μm, thus $\Delta C_F = 0.821 \cdot 10^3$. The measurement uncertainty was estimated based on the ITTC recommendations, equal to 2.5% for the lowest speed case.

Fig. 6 The mesh sensitivity study

The seakeeping experiments of Series 3 were made for two speeds, corresponding to Froude numbers $F_N = 0.11$ and $F_N = 0.22$. The wave height was constant during the experiment and was equal to 0.078 m, corresponding to the value of 1.95 m at full-scale. The wavelength was picked so that it results in encounter frequency equal to a ship's natural heave motions frequency for a given speed. The natural heave frequency of the ship was estimated according to the formula: $\omega_3 = \sqrt{C_{33}/(m + A_{33})}$, where $C_{33} = \rho g A_W$ is a heave restoring force, and A_W is a waterplane area. The coefficient A_{33} can be approximated as m, the ship's mass. The natural heave frequency of the case study vessel estimated by the formula was fn = 0.22 Hz, and the encounter frequency was equal to fe = 0.21 Hz. It corresponded to values of L_{pp}/λ equal to 0.87 for a speed of 5 knots and 1.19 for a speed of 10 knots. The wavemaker generated a sine wave with prescribed parameters. The probe located 15 m from the wave generator recorded the free surface elevation. According to findings from Niklas and Pruszko (2019a), for the speed of v = 5 knots, the added resistance coefficient is in very good agreement with the experimental data (7% difference)—see Table 6. However, the value of the heave transfer function was overestimated by 16%, and the value of the pitch transfer function was underestimated by 12%. For the speed v = 10 knots, the heave and pitch transfer functions correspond to the experimental data very well (2% and 3%, respectively). However, the calculated added resistance coefficient was underestimated by 36%. The performed CFD simulations are in good agreement with the experimental data. Therefore, it was decided that similar numerical models will be used in the presented study of the influence of the wave foil on the ship response.

Experiments were performed in Series 2 and Series 4 for comparison purposes and to gain additional validation data for the numerical model of a hull equipped with wave foils. The towing tank tests were carried out in the same facility,

analogically to Series 1 and Series 3. The matrix of parameters for the experimental cases of all series is presented in Table 4.

The calm water experiments were conducted for the Reynolds number range between 1.1×10^6 and 3.3×10^6, and the Froude Number was between 0.11 and 0.33. The results were extrapolated to the full scale using the ITTC-78 procedure using the ITTC-57 skin friction line and then compared to full-scale CFD simulations. The model's form factor was obtained using the Prohaska method. The calm water experiments of Series 1 and Series 3 were compared to the results of full-scale CFD simulations in Fig. 5. The testing on regular head waves was performed for vessel speeds corresponding to F_N equal to 0.23 (10.4 knots for a full-scale ship) and three wavelengths. These waves were estimated to reach near resonance conditions and are the most demanding cases. A similar approach was used by Simonsen et al. (2013). The heave and pitch motions and total resistance were measured during the experimental study. To compare these results with full-scale seakeeping simulations, they were normalized to obtain each experimental case's added resistance coefficient, heave and pitch transfer functions. The added resistance coefficient σ_{aw} was computed according to the formula:

$$\sigma_{aw} = \frac{F_{xwave} - F_{xcalm}}{\rho g \zeta_{I1}^2 B^2 / L_{PP}}. \tag{5}$$

In the denominator, the symbols being used were: water density ρ, acceleration due to gravity g, and first harmonics of the wave elevation time history ζ_{I1}, which means the wave amplitude, beam B, and length between perpendiculars L_{PP} of the ship. The calm water resistance $F_{x, calm}$ can be extracted from the resistance on the waves $F_{x, wave}$. Both $F_{x calm}$ and $F_{x wave}$ were measured in the x-axis direction. $F_{x wave}$ was calculated using the Fourier Series, which enables the analysis of the force–time history. Each record of

Table 4 The experimental cases of the model-scale tests on calm water and regular wave

Series/case number	Speed v [m/s]	Froude number F_N [–]	Wave height H [m]	Period T [s]	Relative wavelength λ/LPP [–]
1-1	0.50	0.107	Calm water		
1-2	0.60	0.128			
1-3	0.70	0.150			
1-4	0.80	0.171			
1-5	0.90	0.193			
1-6	1.00	0.214			
1-7	1.10	0.235			
1-8	1.20	0.257			
1-9	1.30	0.278			
1-10	1.40	0.300			
1-11	1.50	0.321			
1-12	1.60	0.342			
2-1	0.50	0.107	Calm water		
2-2	0.60	0.128			
2-3	0.70	0.150			
2-4	0.80	0.171			
2-5	0.90	0.193			
2-6	1.00	0.214			
2-7	1.10	0.235			
2-8	1.20	0.257			
2-9	1.30	0.278			
2-10	1.40	0.300			
2-11	1.50	0.321			
2-12	1.60	0.342			
3-1	0.51	0.11	0.078		0.87
3-2	1.02	0.22			1.19
4-1	1.07	0.23	0.06	1.195	1.001
4-2				1.300	1.199
4-3				1.366	1.324

a time-dependent periodical quantity φ may be approximated by Eq. (6).

$$\varphi(t) = \varphi_0 + \sum_{n=1}^{N} \varphi_n cos(2\pi f_e nt + \gamma_n), \, n = 1, 2, 3, \ldots \tag{6}$$

where φ_n and γ_n are the nth harmonic amplitude and corresponding phase, respectively, to calculate the total resistance, the 0th harmonic needs to be calculated from Eq. (7). This corresponds to the average value of resistance time history (Tezdogan et al. 2015).

$$\varphi_0 = \frac{1}{T} \int_0^T \varphi(t)dt. \tag{7}$$

The heave and pitch transfer functions are expressed by Eqs. (8) and (9):

$$TF_{x3} = \frac{x_{31}}{\zeta_{I1}}, \tag{8}$$

$$TF_{x5} = \frac{x_{51}}{k\zeta_{I1}}. \tag{9}$$

k means the wave number and the product $k\zeta_{I1}$ is the wave slope. For the numerical simulations and towing tank experiments, at least ten periods of ship motion were analyzed after signal stabilization to compute the mean value of the ship response amplitudes and the total resistance.

Table 5 Simulation cases of the full-scale CFD on calm water and regular wave

Case number	Speed v [kn]	Froude number F_N [–]	Wave height H [m]	Period T [s]	Relative wavelength λ/LPP [–]	Remarks
1	5.0	0.11	Calm water			
2	7.0	0.15				
3	9.0	0.20				
4	10.4	0.23				
5	12.0	0.26				
6	13.0	0.28				
7	15.0	0.33				
8	10.4	0.23	1.5	5.975	1.001	
9				6.500	1.199	
9a				6.500	1.199	$+ 5^0$ AoA
9b				6.500	1.199	$- 5^0$ AoA
10				6.830	1.324	
11				7.165	1.439	
12				7.570	1.606	
13				8.360	1.959	

Fig. 7 Model with hydrofoils prepared for towing tank testing

4.3 Simulation cases for model scale CFD: seakeeping validation study

The validation study was performed in the model scale for three selected cases, representing the most challenging conditions of dynamic ship motions in close to resonance conditions and significant wave loads.

The validation scope compared total resistance on waves, heave and pitch motion for wave lengths λ/LPP = 1.001, λ/LPP = 1.199 and λ/LPP = 1.324 and model speed equal to 1.07 m/s. The wave height was equal to 0.06 m. Therefore, those conditions corresponded to cases 4-1, 4-2 and 4-3, presented in Table 4.

The validity of the model without hydrofoils was already proven, and here the focus is on the validation of ship motion and resistance solely for the ship with hydrofoils.

4.4 Simulation cases for the full-scale CFD

Simulations on the regular head wave were performed for a wave height equal to 1.5 m, corresponding to sea state 4 on the Douglas scale. The vessel's speed was equal to 10.4 knots (F_N = 0.23). The simulations were performed for a wide range of wavelengths while keeping the wave height constant. Similar cases were analyzed for the vessel in an 'as built' condition and equipped with wave foils. At first, the calm water simulations were performed to calculate the added resistance from the total resistance in the second stage of the analysis. The calm water simulations were performed for the range of Froude Number F_N = 0.11 to F_N = 0.33 (ship speed from 5 to 15 knots) for both models: with and without wave foils. The analyzed numerical simulation cases are presented in Table 5. The influence of the hydrofoil angle was also checked for the selected wavelength (λ/LPP = 1.199). The angle of attack (AoA) equal to + 5 degrees and − 5 degrees corresponds to Case 9a and Case 9b, respectively. The remaining simulations were performed for the angle of attack equal to 0 degrees.

5 Results and discussion

5.1 Calm water

The ship model's resistance on calm water was analysed to determine the added resistance in the later analyzed wave design cases. The results of numerical calculations and

Fig. 8 Total resistance of the ship in calm water, with and without the hydrofoils, as determined by towing tank experiments (EFD) and full-scale CFD simulations
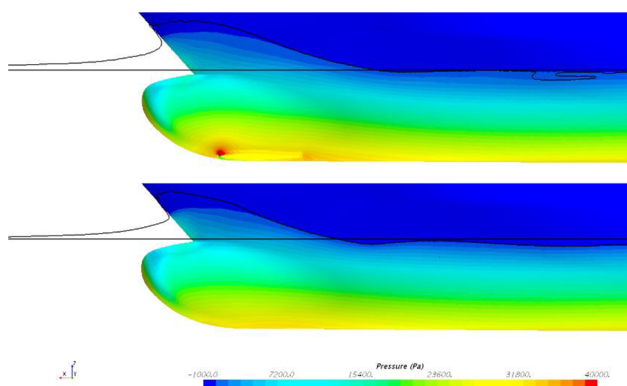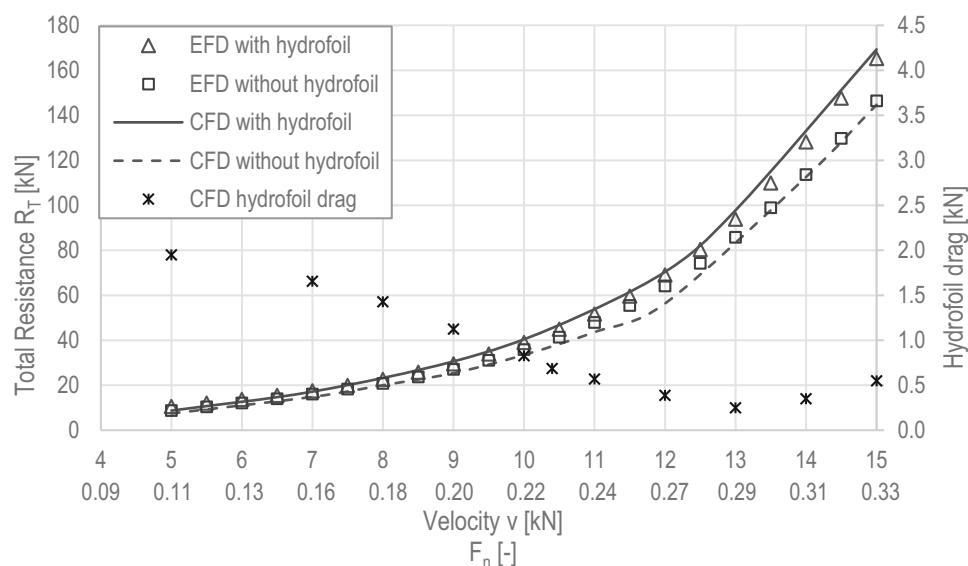

Fig. 9 Comparison of pressure distribution on hull surface without and with the hydrofoil at a speed of $F_N = 0.26$

experimental tests for the ship model, with and without a hydrofoil, are shown in Fig. 7. On the right axis, the drag of the hydrofoil itself was plotted. This comparison aimed to validate the computations and assess the influence of wave foil on the value of the ship's total resistance on calm water.

According to Fig. 7, and as expected, the presence of a hydrofoil significantly increases the calm water resistance, which agrees with experimental results. This is also in line with the conclusions indicated by the other authors mentioned in the literature review presented in Sect. 1. Adding a fixed hydrofoil in the bulbous bow section increased the total hull resistance by 17% for low-speed cases, referring to Froude Numbers between $F_N = 0.11$ and $F_N = 0.15$ (a speed of 5 knots and 7 knots). The rise of total resistance for a speed of $F_N = 0.20$ and $F_N = 0.23$ (9 knots and 10.4 knots) was equal to 21%. For the speed of $F_N = 0.26$ (12

knots), it was 24%. The shear drag increased by 4–6% for all cases; however, the pressure resistance increased by around 40%. For the calm water simulation, the uncertainty analysis and verification of the numerical model were presented in Niklas and Pruszko (2019b) and are intentionally not reproduced here. Very good agreement was obtained between the experimental and numerical results. Except for the speed of 5 knots (when CFD underestimated the total resistance by 17%), the remaining speed differences were smaller than 4% and for a design speed of 10.4 knots, it was equal to 1.28%. It is interesting to see the decrease of the hydrofoil drag with the increasing speed. The first reason is that the vessel trim angle changes from 0.5 degrees bow down for a speed of 5 knots to 0.2 degrees bow down for 13 knots. The pressure drag component for higher speed is negative—producing the thrust force. However, it does not suppress the hydrofoil shear resistance.

The interaction between the hull and hydrofoil was investigated to identify the reason for increased resistance. Figure 8 compares the pressure distribution on the hull surface for a ship without and with a hydrofoil at a speed of $F_N = 0.26$ (12 knots). As expected, a high-pressure area occurred around the foil (Fig. 9).

In addition, the influence of a hydrofoil on the wave pattern was checked. The comparison of free surface elevation for the ship's speed of $F_N = 0.26$ (12 knots) is presented in Fig. 10. Slightly higher bow waves can be observed for the bulbous bow equipped with the hydrofoil. The flow direction around the bulbous bow causes suction on the bottom side, whereas the top surface of the foil is a higher pressure side. A high bow wave resulted in a more significant elevation of divergent waves.
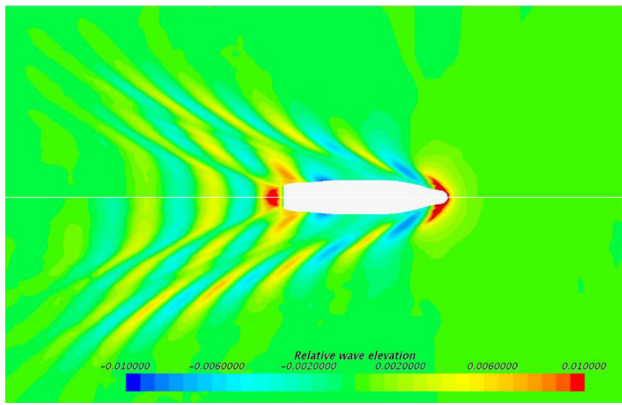
Fig. 10 Wave pattern for the ship speed of $F_N = 0.26$ for the ship 'as built' (top half) and equipped with the hydrofoils (bottom half)
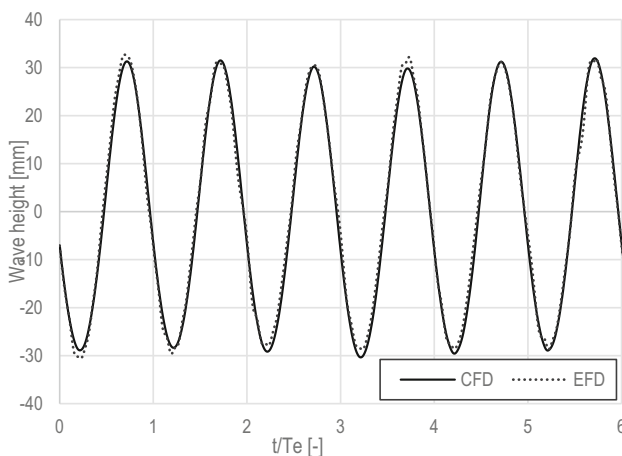

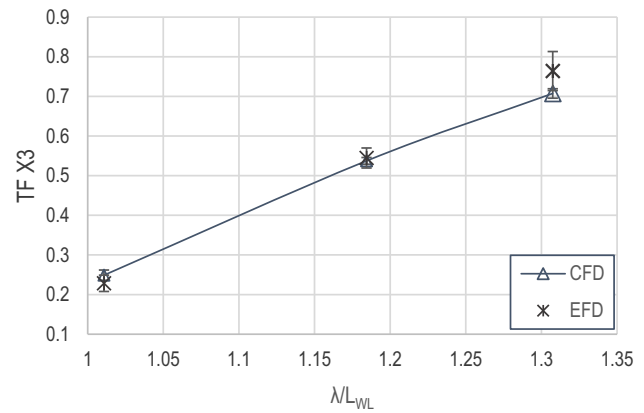**Fig. 11** Comparison of wave elevation—validation study

Fig. 12 Comparison of heave transfer function—validation study

Fig. 13 Comparison of time history for heave motion for the λ/LWL = 1.2

5.2 Regular wave–validation study

To monitor the parameters of the incoming waves for CFD simulations, the position of the free surface was tracked in front of the model bow. Figure 11 presents the comparison of the time history of the wave elevation for CFD and EFD for the wavelength $\lambda/L_{WL} = 1.2$. During the towing tank experiments, the wave probe was fixed to the tank wall at a distance of ¼ basin length away from the wave generator. Therefore, to compare wave elevation in the CFD and EFD, obtained results are presented concerning the period of encounter t/Te.

In Fig. 12, the comparison of the heave transfer function obtained from the towing tank experiments and model-scale CFD seakeeping simulations for three different wavelengths is presented. The validation was carried out for the model equipped with the bow hydrofoil. For wave $\lambda/L_{WL} = 1.01$, the values of heave transfer functions obtained by EFD are smaller than the CFD results. A very good agreement is obtained for the medium wave, and CFD under-predicts

heave motion amplitude for the most extended analysed wave. The uncertainty of heave motion amplitude obtained by towing tank test was equal to 9%, 5% and 6% for the shor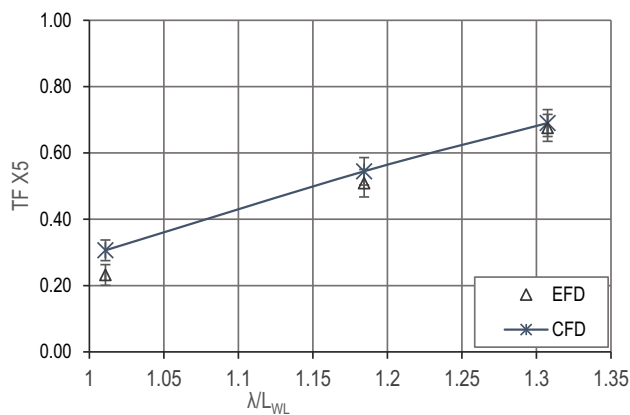test, medium and most extended waves, respectively. For CFD, those values were equal to 5%, 2% and 2%. The error bars were included in the plot.

Figure 13 presents the time history of the heave motion obtained numerically and experimentally for the $\lambda/LWL = 1.2$. It can be seen that good agreement between the experiment and simulations was obtained.

The pitch transfer functions are presented in Fig. 14. It can be seen that the numerical simulations in the model scale over-predicted the pitch motions for the entire range of analyzed wavelengths. The agreement between experimental and numerical results improves as the wavelength increase. Good agreement was achieved for the wavelength equal to $\lambda/L_{WL} = 1.32$; the discrepancy was equal to 3.2%. The uncertainty of pitch motion amplitude obtained by towing tank test was equal to 13%, 8% and 6% for the shortest, medium and most extended waves, respectively. For CFD,

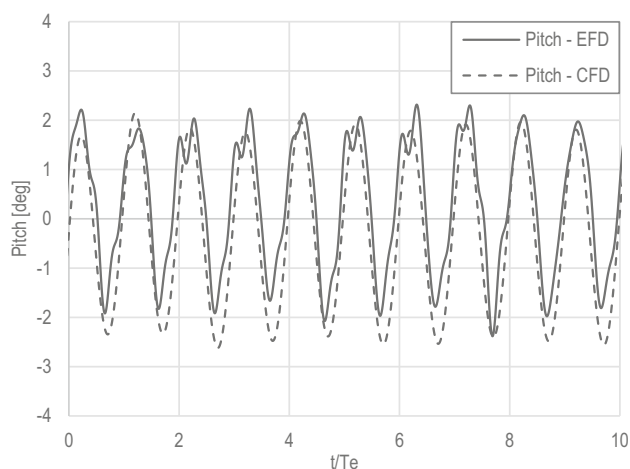**Fig. 14** Comparison of pitch transfer function—validation study

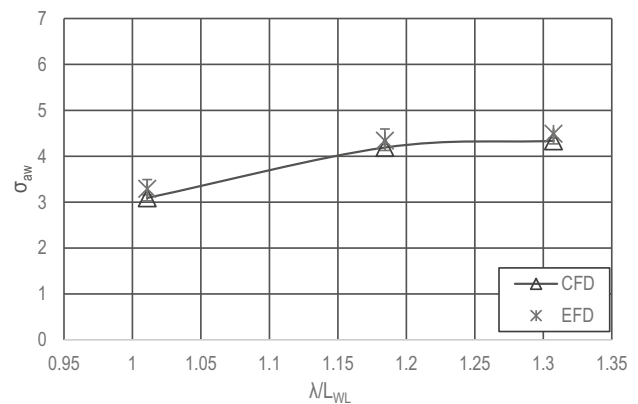**Fig. 15** Comparison of time history for pith motion for the $\lambda/L_{WL} = 1.2$

Fig. 16 Comparison of added resistance coefficient—validation study

The comparison of the added resistance coefficient, obtained numerically and experimentally, is presented in Fig. 16. The CFD method slightly under-predicted resistance for the entire range of analyzed wavelengths. The difference between the experimental and numerical results was relatively small, oscillating between 6% and 3.5%. The uncertainty of added resistance coefficient obtained by towing tank test was equal to 7%, 5% and 5% for the shortest, medium and most extended wave, respectively. For CFD, those values were equal to 2%, 1.5% and 1.5%. The error bars were included in the plot.

Table 6 summarizes the comparison of the numerical and experimental results. The difference was calculated in percentages as a discrepancy between the numerical results concerning the value of empirical predictions. In general, the agreement between numerical and experimental results was very good.
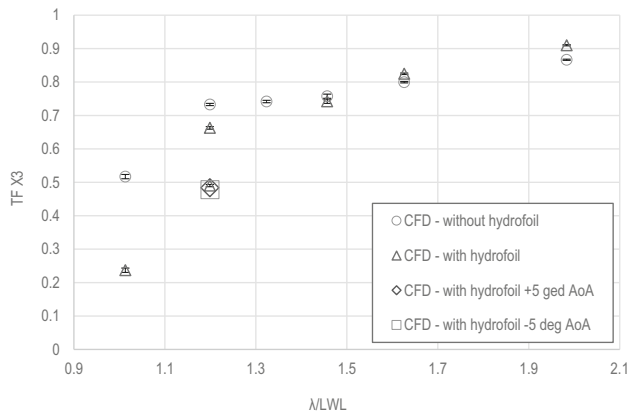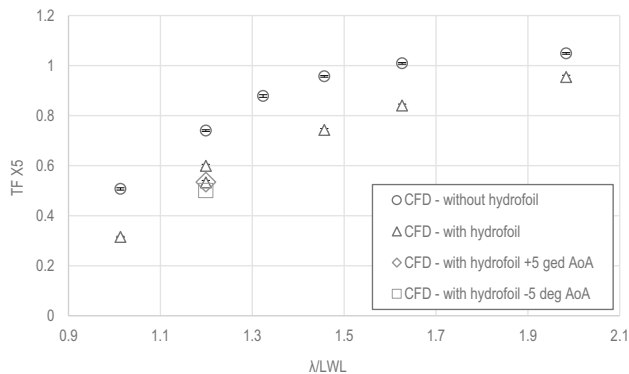
Considering experimental resistance uncertainty for all analyzed waves, the differences in the EFD and CFD results are below the experimental uncertainty. For pitch motions, the amplitude is highly overestimated for the shortest wave. However, for the remaining wavelengths, the results are within experimental uncertainty. For heave motions, the Case 8 results are within experimental uncertainty. Although the validation was not obtained for all presented cases and measures, it is believed that considering the dynamic nature of the analyzed physics phenomena, the presented numerical model should be regarded as valid and credible.

5.3 The influence of adding the bow hydrofoils on heave, pitch, and added resistance: a case study

Figure 17 compares a heave transfer function obtained by the full-scale CFD simulations for the vessel without a hydrofoil (as-built) and with the hydrofoil in the range of wavelengths between $\lambda/L_{WL} = 1.01$ and $\lambda/L_{WL} = 1.98$. For wavelengths

those values were equal to 6%, 3% and 2.5%. The error bars were included in the plot.

In Fig. 13, the direct comparison of the time history of the pitch motion obtained numerically and experimentally for the $\lambda/L_{WL} = 1.2$ is presented. The pitch motions time history signal obtained experimentally is more noisy and irregular than the numerical one. The agreement between the experiment and simulation is believed to be good, considering the rough waves and near-resonance conditions. The non-linear responses of pitch motions for EFD result from used measuring devices, which were inclinometer mounted at the COG of the model, remaining recorded signals—i.e., resistance and heave had smoother shapes. For the presented wavelength, very rapid and dynamic motions of the model were observed, which also increased the uncertainty of measurements (Fig. 15). Observing partially non-linear signals in measurements for close-to-resonance conditions is not unusual. For the longer wavelengths obtained time history of pitch motions had more regular character.

Table 6 Relative difference between experimental and numerical results of the heave transfer function, pitch transfer function, and the added resistance

Case Id	λ/L_{WL}	$\frac{TF_{X3(exp)}-TF_{X3(CFD)}}{TF_{X3(exp)}}$	%D EFD TF_{X3}	$\frac{TF_{X5(exp)}-TF_{X5(CFD)}}{TF_{X5(exp)}}$	%D EFD TF_{X5}	$\frac{\sigma_{aw(exp)}-\sigma_{aw(CFD)}}{\sigma_{aw(exp)}}$	%D EFD σ_{aw}
7	1.013	8.9%	9.1%	32.3%	13%	− 6.0%	7%
8	1.199	− 1.3%	5%	7.1%	8%	− 3.5%	5%
9	1.324	− 7.2%	6%	2.1%	6%	− 3.5%	5%

Fig. 17 Effect of the bow hydrofoils on the heave transfer function of the case study ship

Fig. 18 Effect of the bow hydrofoils on the pitch transfer function of the case study ship

up to $\lambda/L_{WL} = 1.5$, the bow foil causes a significant reduction of heave motion, whereas, for longer waves, the vertical motions of the vessel without a foil are slightly smaller. For the wave $\lambda/L_{WL} = 1.2$, additional simulations were performed for the foil angle of attack equal to + 5 degrees and − 5 degrees. In this case, a negligible effect on the heave motions was observed.

Figure 18 compares a pitch transfer function obtained by the full-scale CFD simulations for a vessel without and with the hydrofoil in the range of wavelengths between $\lambda/L_{WL} = 1.01$ and $\lambda/L_{WL} = 1.98$. The presence of hydrofoil reduces

the pitch motion of the ship in the entire range of analyzed wavelengths. The most considerable reduction was observed for the shortest analyzed wavelength ($\lambda/L_{WL} = 1.01$) and had a significant favourable influence up to a wavelength of $\lambda/L_{WL} = 1.55$. As the wavelength increased, the effect of pitch reduction decreased. For the wave $\lambda/L_{WL} = 1.2$, additional simulations were performed for the foil angle of attack equal to + 5 degrees and − 5 degrees. In this case, a negligible effect on the pitch motions was observed.

At this point, it is worth discussing the scale effect in the damping motions for the vessel equipped with the hydrofoil. CFD calculations were performed for three selected wavelengths for both model and full scale. In principle, the scale effect is negligible for ship motions. Scaled heave motions differed by about 5%, whereas the pitch angles were almost identical and lay within the numerical uncertainty. In principle, the full-scale motions were smaller. Therefore, the model tests and model scale CFD are credible sources of information about the damping of motions using hydrofoils in ship scale. A more extensive study would have to be performed to address the resistance problem. However, it seems that the scale effect will be more significant for resistance due to differences in boundary layer thickness between the model and full-scale ship and different relations to pressure and viscosity forces for ship and model. Moreover, the resistance cannot be as directly compared and additional uncertainty arises.

Several aspects need to be considered when analyzing the influence of the hydrofoils on the ship motions presented in the normalized form in Figs. 17 and 18. The effect of reducing pitch motions is apparent. It is worth noting that the pitch and heave motions are coupled, and reduced pitch motions to some extent, help to minimise heave motions. Figure 19 explains the differences in heave and pitch motions for the shortest wave (Case 8), and it presents a similar moment of periodic ship motions. The colour range depends on the Z-position of the free surface elevation, and dark blue corresponds to the trough and red to the crests. It can be noticed that the bow part of the vessel with hydrofoil (on the right) is significantly less immersed, and the red oval underlines it. Moreover, different local wave systems around the ship seem to create the vessel's local crest with hydrofoil, strengthening the effect of reduced heave motions—underlined by a green oval.
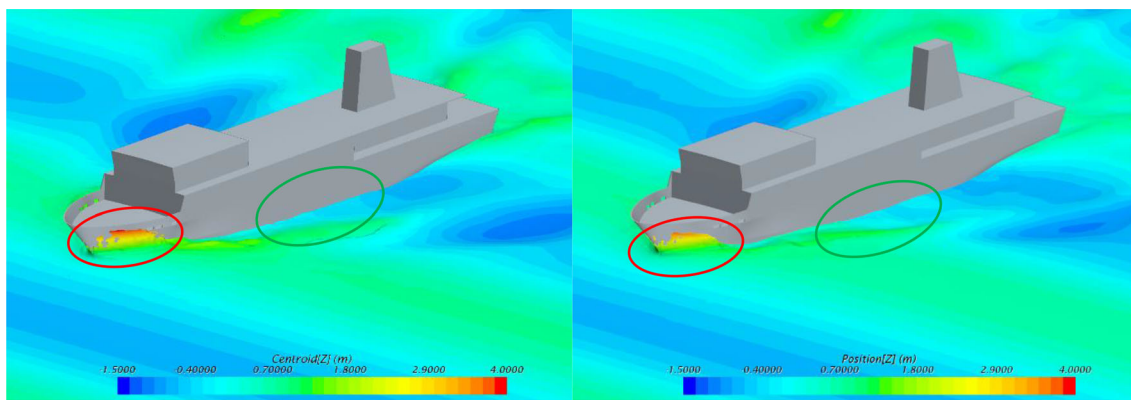
Fig. 19 Wave system around the vessel without hydrofoils (on the left) and with hydrofoils (on the right)
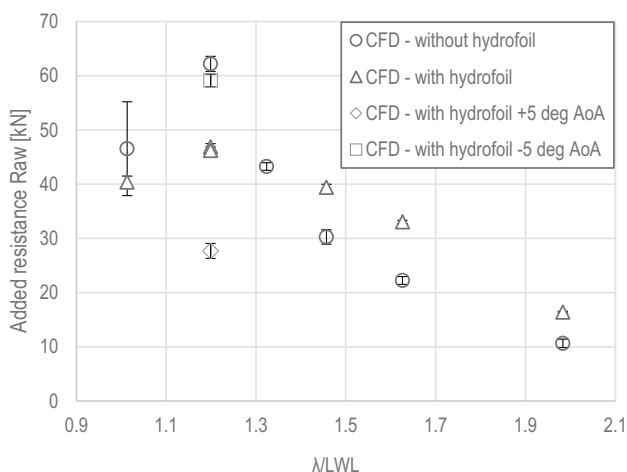

Fig. 20 The effect of bow hydrofoils on added resistance on regular waves

The results can also be analyzed concerning the generalized equation of the ship's motion. Three reaction forces (moments) are present: inertial, damping, and restoring forces. For low-frequency waves, the restoring forces are dominant. The damping is crucial for middle-length waves, whereas the inertial forces are the most influential for long waves. The heave and pitch motions are heavily reduced for short and middle waves due to significantly increased damping caused by the presence of the hydrofoil. The most probable reason for the slight increase in heave motions for the vessel with a bow hydrofoil in the long waves is water added mass increase compared to the vessel as-build. For the pitch motions, increased damping seems to dominate over the increased moment of inertia. Therefore the pitching motions are reduced for the entire range of analyzed wavelengths.

Figure 20 compares added resistance, determined by full-scale CFD simulations for the vessel without and with the hydrofoils. The bow hydrofoil very effectively dampens the peak of total resistance for a wavelength equal to λ/L_{WL}

= 1.19. The maximum total resistance value for the vessel equipped with the hydrofoils occurred for a wavelength equal to λ/L_{WL} = 1.25 and was significantly smaller. However, both curves cross at a wavelength equal to λ/L_{WL} = 1.30. For longer waves, the application of hydrofoils increased the total resistance of the case study ship.

For the wave λ/L_{WL} = 1.19 and the hydrofoil with the angle of attack equal to + 5 degrees massive reduction of added resistance was observed (by 56%). In contrast, the − 5 degrees angle of the attack hydrofoil caused an increase in the added wave resistance. For the vessel without hydrofoils, greater immersion of the bow (see Fig. 17), potentially much higher pressure loads due to waves, and higher impact of the ship crashing the incoming wave explain a significant reduction of added resistance for a vessel equipped with the hydrofoils—additionally, reduced motion results in decreased resistance for short and middle waves. However, for long waves, increased pressure and shear resistance overwhelm the effect of lowering motions. The plots of resistance generated on the hydrofoils are presented to understand the increase of the resistance for the longer waves. Figure 19 shows the drag of the hydrofoil on waves. It can be noticed that the hydrofoil for all analysed cases, except the one with the angle of attack of + 5 degrees, produces drag. It explains why the added resistance due to waves is so tiny for the hydrofoil with 5 degrees angle of attack compared to other tested cases. This finding shows that this solution has great potential, and future research can optimize the angle of attack for different conditions. It is also worth noting that the resistance of the hydrofoil increases for longer waves. This is one of the reasons for the increased wave-induced additional drag for a ship equipped with hydrofoils.

Figure 21 presents the plot of the hydrofoil added drag due to waves. The added drag acting on the hydrofoils was calculated as follows:
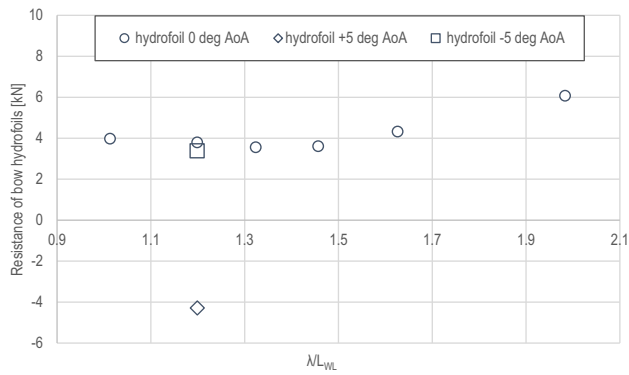
$$D_{added} = D_{wave} - D_{calm}. \tag{10}$$

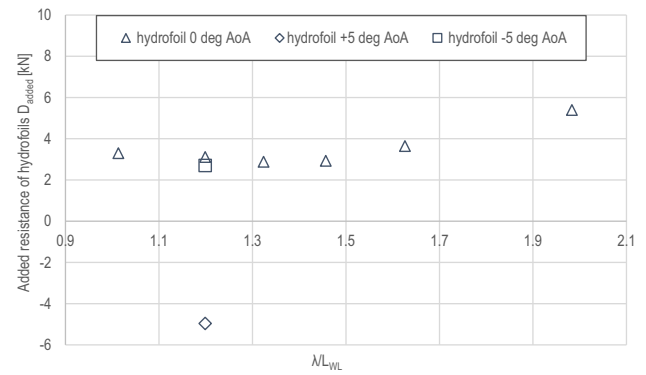**Fig. 21** Resistance of bow hydrofoils on regular waves

Fig. 22 Added wave drag of bow hydrofoils on regular waves

The value of D_{wave} has been averaged over ten periods, whereas D_{calm} is the drag of the hydrofoil on the calm water. According to Fig. 7, it is equal to 0.68 kN. According to Fig. 20, the presence of hydrofoils for waves shorter than $\lambda/L_{WL} = 2$ is relatively neutral and does not cause an increase in added resistance. For the most extended analysed wave $\lambda/L_{WL} = 1.96$, there is a visible increase of an added wave resistance generated by the foil presence. Moreover, the added wave resistance significantly reduces for the foil

having an angle of attack equal to 5 degrees. This explains the source of such a substantial reduction in the ship's resistance. Figure 22 also presents increased ship resistance for the most extended analysed wave.

Figure 23 shows the net force vectors for a hydrofoil with an angle of attack AoA of 5 degrees to visualise the effect of hydrofoils during various phases of ship motion. The top two pictures show the phase of the motion when the bow is pitching up. The horizontal component propelling the vessel
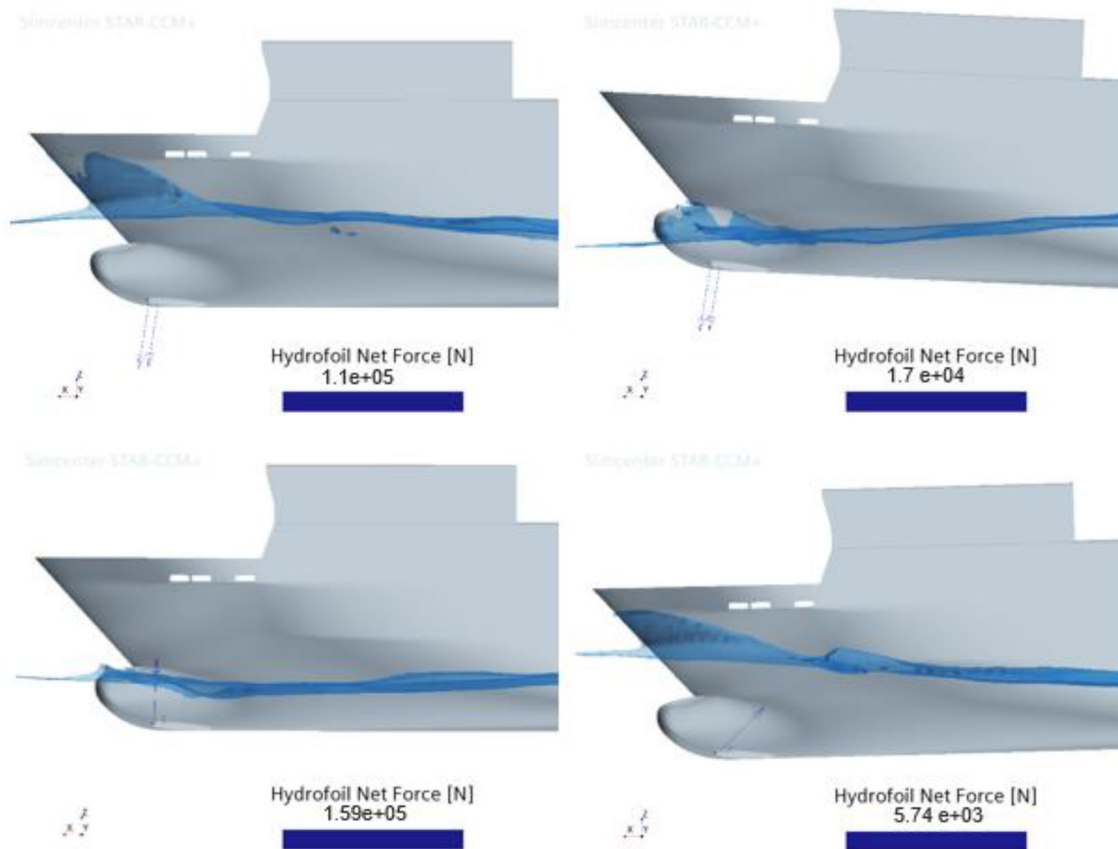

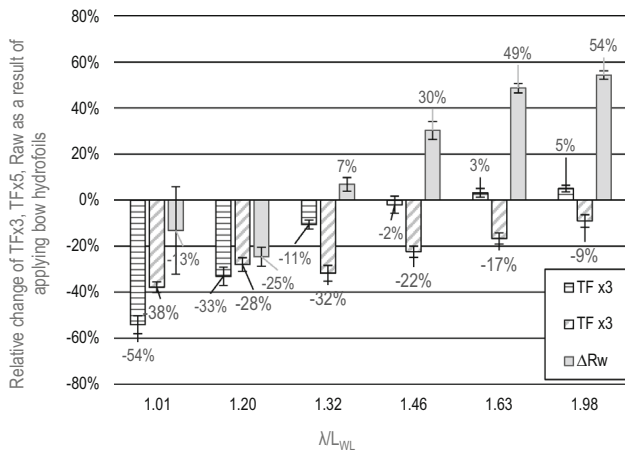**Fig. 23** Net force vector for hydrofoils at 5 deg AoA with bow pitching up (top) and pitching down (bottom)

Fig. 24 Effect of adding bow hydrofoils (AoA = 0 deg) on heave (TF × 3), pitch (TF × 5), and added resistance (raw)
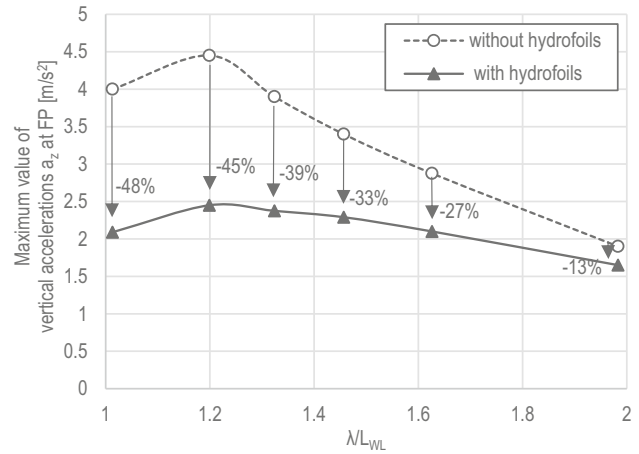

Fig. 25 Vertical acceleration at the fore perpendicular (FP) for the ship without and with hydrofoils (AoA = 0 deg)

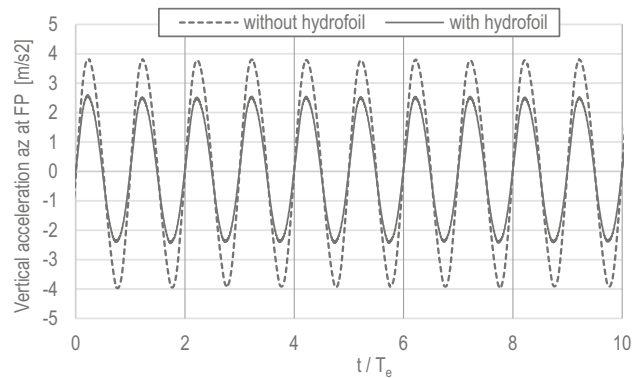Fig. 26 Effect of the wave foil on the vertical acceleration at the fore perpendicular for the wavelength λ/L = 1.3

may be observed. The two bottom pictures present the force direction while the vessel's bow is pitching down. The drag force component is the most significant then.

Figure 24 presented the percentage difference between the motions and added resistance of the vessel with bow hydrofoils, compared to the original design. In the example, the percentage difference for an added resistance R_{aw} was calculated using the equation:

$$R_{aw} = \frac{(R_{aw(withhydrofoil)} - R_{aw(withouthydrofoil)})}{R_{aw(withouthydrofoil)}} 100\%. \quad (10)$$

For wavelengths $\lambda/L_{WL} = 1.01$ to $\lambda/L_{WL} = 1.3$, a very beneficial effect of the hydrofoils can be observed. It was the most pronounced at wavelength $\lambda/L_{WL} = 1.2$, for which heave motion decreased by 33%, pitch motion decreased by 28%, and additional resistance decreased by 25%. For waves longer than $\lambda/L_{WL} > 1.32$, the effect of damping the ship motions progressively reduced, and the added wave resistance increased significantly. Due to numerical uncertainty for $\lambda/L_{WL} = 1.42$, hydrofoils' positive or negative effect on heave motion cannot be assessed. For wave $\lambda/L_{WL} = 1.01$, the uncertainty of added resistance for a vessel without foil is very high, so for the same reason, it is not evident that the hydrofoils are beneficial.

Another significant effect of using hydrofoils in offshore wave conditions is reduced vertical hull accelerations. Figure 25 shows the impact of hydrofoils on the maximum acceleration at the ship's fore perpendicular (FP) for different wavelengths. The reduction of maximum acceleration is principal. The most significant values of − 48% and − 45% were for the wavelengths $\lambda/L_{WL} = 1.01$ and $\lambda/L_{WL} = 1.2$, accordingly. The minimum reduction was equal to − 13% and corresponded to the wavelength $\lambda/L_{WL} = 1.98$. The sample time history of the accelerations at the fore perpendicular

FP for wavelength $\lambda/L_{WL} = 1.32$ is presented in Fig. 26. The time was normalized by the value of encounter period T_e.

To analyze whether the foil reaches the stall angle, the time history of the generated lift was analyzed. Several cases were considered, including the longest waves at which the highest amplitude of pitch motion occurred and the wave with a length of $\lambda/L_{PP} = 1.19$, for which the maximum amplitude of lift was observed. Time histories of lift are presented in Fig. 27. A sudden loss of lift was not found for any of the waves.

To provide a more detailed analysis of the motion and forces generated by the hydrofoil, selected critical load cases in the time domain are presented below. Figure 28 corresponds to Case 9, where the effect of the foil was found to be the most positive, whereas, Fig. 29 corresponds to Case 13 for the most extended wave and the purely unfavourable impact of the hydrofoil. Negative values of thrust force mean that the foil produces additional resistance instead of a propelling force. The water surface was the reference point for tracking the foil's vertical position.

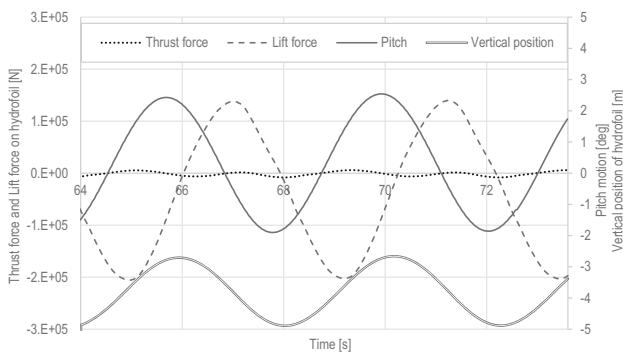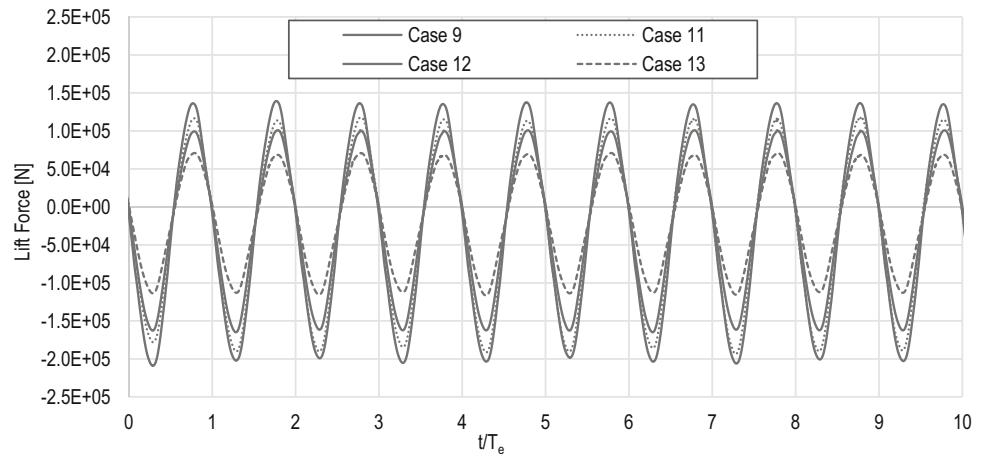**Fig. 27** Time history of the lift generated by the wave foil for the wavelength $\lambda/L = 1.2$ (Case 9)

Fig. 28 Time history of the vertical hydrofoil position, pitch, lift, and thrust forces generated by the wave foil—Case 9
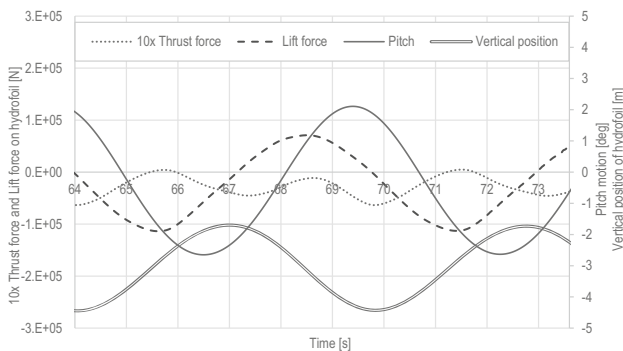

Fig. 29 Time history of the vertical hydrofoil position, pitch, lift, and thrust forces generated by the wave foil—Case 13

It can be seen that the plots presented in Figs. 28 and 29 have several features in common. The highest drag of the hydrofoil occurs when the foil is in a maximum downward position, and the second local minimum corresponds to the maximum upward position of the foil. The maximum value of lift force acting upwards or downwards corresponds to the pitch angle close to zero. At these points, heave motion

corresponds closely with its equilibrium position. To investigate the physics of the thrust and lift forces generated by the hydrofoil more deeply, the selected repetitive segment of the ship's motion is shown in Fig. 30, together with the values of the lift and thrust forces.

It can be seen that zero thrust force occurs close to the pitch equilibrium and for the maximum value of a pitch angle. The maximum value of thrust force occurs when the ship approaches the maximum pitch angle with a bow downwards position. The maximum local value of a drag force generated by hydrofoils, equal to the opposing thrust force, occurs after reaching the ship's maximum pitch angle. The lift force was generated vertically upwards or downwards concerning the 'bow up' or 'bow down' position. The maximum value of lift force correlated to the pitch equilibrium position. Minimum lift forces were observed at the minimum and maximum pitch angle values.

Figure 31 shows the time history of the force along the X-axis, the ship's pitch angle, and the vertical position of a hydrofoil. Based on this picture, additional information might be gained, as coupled relations between vertical velocity and lift and thrust forces were observed. The local maximum thrust force occurs close to the time intervals in which the vertical velocity of the hydrofoil reaches its local extrema. The local maxima of lift force corresponded to the local maxima of the vertical velocity plot of the hydrofoil. The water surface was the reference point for tracking the foil's vertical position.

5.4 Effect of hydrofoil structural stiffness on the hydrodynamic flow

Generally, the hydrodynamic flow generated on the foil depends on its deformability. This raises the question of the need for fluid–structure interaction (FSI) simulations for hydrofoils, especially slender ones. It should be addressed carefully in each design. In this study, the structural response

Fig. 30 Relation between the pitch angle, lift, and thrust forces for Case 9 ($\lambda/L_{PP} = 1.19$)
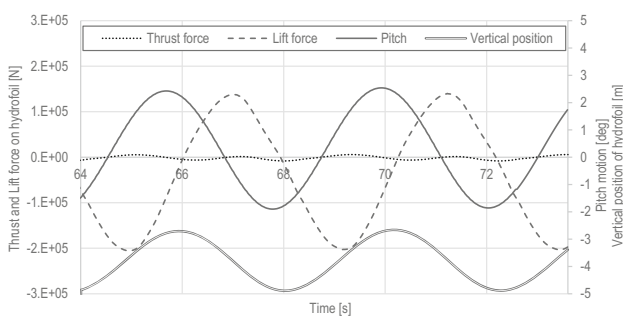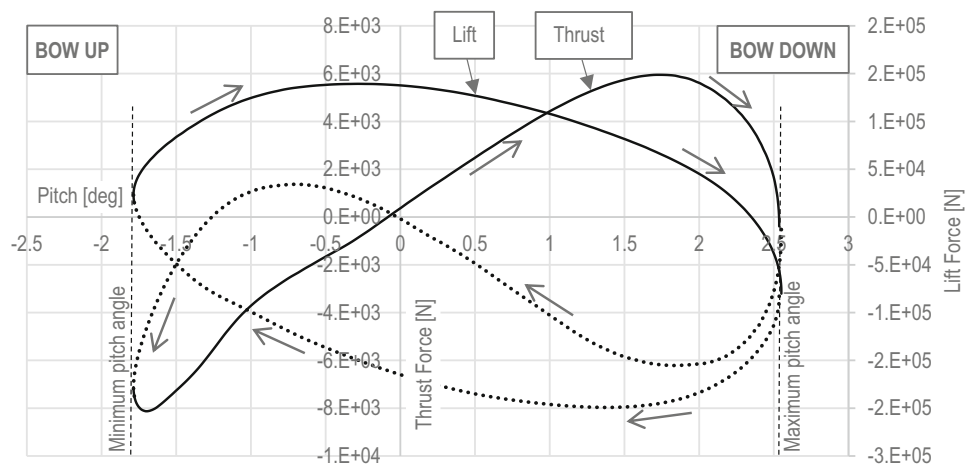

Fig. 31 Time history of the thrust force, vertical velocity, and pitch angle—Case 9

of the hydrofoils due to hydrodynamic loads was investigated by the finite element analysis (FEA). Structural analysis was carried out with the Nastran solver. The goal was to calculate the maximum deformation of foils due to the hydrodynamic loads previously estimated by the CFD simulations. The maximum vertical force applied to the foil surface was 2e5 N, according to Fig. 25. In this static analysis, inertial forces have been omitted due to the dominant role of hydrodynamic loads. The structure of the hydrofoil was modelled by 4-noded quadrilateral finite elements with 6 degrees of freedom in each node.

The boundary conditions are assumed to block the foil's edge inside the hull. In the model representation, the foil edge at the hull was restrained. For simplicity, the analysis assumes that the foil is made of a standard 20 mm thick steel plate with a Young modulus of 2E5 MPa and a Poisson ratio of 0.3. No internal stiffeners were considered here for simplification. For the maximum vertical hydrodynamic forces, the calculated maximum deformations of the foil were equal to 30 mm—see Fig. 32. The unreformed model was included as a wireframe. The foil span is equal to 3 m. Thus, the maximum deformation of the foil is equal to only 1% of the span. As a consequence, the deformability of the foil may be omitted in the hydrodynamic analysis. Although the
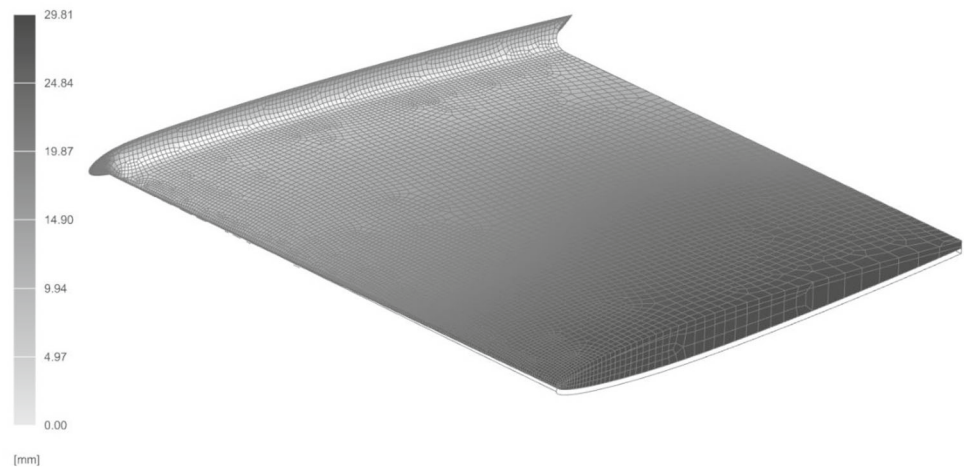
detailed design of the foil structure is not the subject here and is included in the retrofitting procedure presented in the following section.

6 Procedure for hydrofoil assessment in the retrofitting of existing ships

This section presents a proposal for the procedure to assess the impact of applying hydrofoils on the ship's performance (as well as the economic and environmental aspects). The procedure shown in Fig. 31 contains three main steps that enable a decision on the appropriateness of the solution under analysis. The procedure starts with the determination of initial ship performance in operational conditions. The main technical characteristics are added wave resistance, ship motions, and accelerations. Three different determination methods are proposed: full-scale CFD simulations, towing tank experiments, and onboard measurements. Full-scale CFD simulations, supported by towing tank testing, are the most effective.

In the next step, for analogous cases, characteristics are determined for the ship with added hydrofoils. This makes it possible to assess the effect of the hydrofoils on the added wave resistance and ship motions. This step includes an internal loop of a hydrofoil design and integration into a ship's structure. The design of the hydrofoil may be simplified to a simple selection of the hydrofoil having proofed performance, as presented here. However, a ship-specific hydrofoil optimization process may be performed, bringing higher performance. Hydrofoil design typically includes computer simulations, like computational fluid dynamic (CFD) and structural finite element analysis (FEA). If the foil undergoes significant deformation under loads, it can affect the hydrodynamic flow around the foil. It is then necessary to perform a coupled analysis, namely the fluid-structure interaction (FSI)

Fig. 32 Maximum deformations of the hydrofoil calculated by FEA [mm]

simulations. The test results showed that improved seakeeping performance is due to the suppression of vertical motion. Any streamlined foil shape serves this function, and using more thin foils will likely bring more durability problems than drag reduction benefits. However, this is a subjective comment unsupported by research results today. Detailed research on hydrofoil optimization will be presented in a future dedicated study. In the second stage of this procedure, the methods of full-scale CFD, supported by towing tank testing, are recommended to be used. The full-scale CFD simulations presented in this paper were performed using high power computing (HPC) and commercial software. Discussion on similar simulation performance is included in Sect. 4.1 (Niklas and Pruszko 2019a).

The procedure's third step is retrofitting's impact on economic and environmental aspects. Capital expenditure (CAPEX) and operating expenditure (OPEX) are typically evaluated, and emissions assessment also plays an important role. Finally, a synthetic analysis based on specific economic and environmental indicators allows for the evaluation of retrofitting (Fig. 33). If a solution does not meet the indicated criteria, it is possible to perform a new design iteration in step 2 for the changed design parameters. The proposed procedure is formulated in general terms and applies to different types of ships and retrofitting technology.

7 Conclusions

Due to the long lifespan of ships (about 30 years), retrofitting the existing fleet has excellent potential for increasing energy efficiency and reducing emissions in maritime transport. Reduced fuel costs, improved safety, and comfort are equally important. This study presented an analysis of the application of bow hydrofoils for a case study ship. Selected seakeeping performances were analysed, like hull motions and wave-added resistance. The work was carried out for the

operational speed of the vessel and a regular bow wave of different lengths. Investigations were carried out in both a towing tank and by full-scale CFD simulations. The results were compared for a ship without and with hydrofoils under identical sea wave conditions. The retrofitting of the analyzed ship by installing the bow hydrofoils significantly reduced hull motions and wave-added resistance for the wavelengths ranging from $\lambda/L_{WL} = 1$ to $\lambda/L_{WL} = 1.25$.

The most beneficial effect of hydrofoils was observed for a wavelength $\lambda/L_{WL} = 1.20$. The reduction of heave motion was equal to 33%, pitch motion was equal to 28%, and the reduction of wave-added resistance was equal to 25%. The damping force component generated on the hydrofoil has a value of more than ten times the horizontal component. The horizontal component can be interpreted as thrust (in the direction consistent with the ship's motion) or drag (in the opposite direction). Thus, the main benefit of using hydrofoils, in this case, is suppressing longitudinal pitch motion, which reduces added wave drag. For the wavelength $\lambda/L_{WL} = 1.20$ changing the foil's angle of attack by 5 degrees, the reduction of wave-added resistance was as much as 56% due to a thrust force generated on the foil. A significant increase in comfort and safety may also result from using hydrofoils due to reduced vertical accelerations. The reduction in maximum accelerations was observed for all cases analyzed and ranged from 48% for $\lambda/L_{WL} = 1$ to 13% for $\lambda/L_{WL} = 2$. Outside the $\lambda/L_{WL} = 1$ to $\lambda/L_{WL} = 1.25$ wavelength range, the impact of hydrofoils is strongly negative. Using hydrofoils in calm water is detrimental because it significantly increases total resistance. Thus, when analyzing the validity of the use of hydrofoils, it is crucial to determine the operational conditions under which their use is beneficial. Future research may address other aspects, such as reducing hull motions' impact on collision effects. Improved manoeuvrability may also be addressed. A universal procedure was presented for selecting hydrofoils for existing ships using full-scale CFD simulations. It is an effective tool to determine their effect
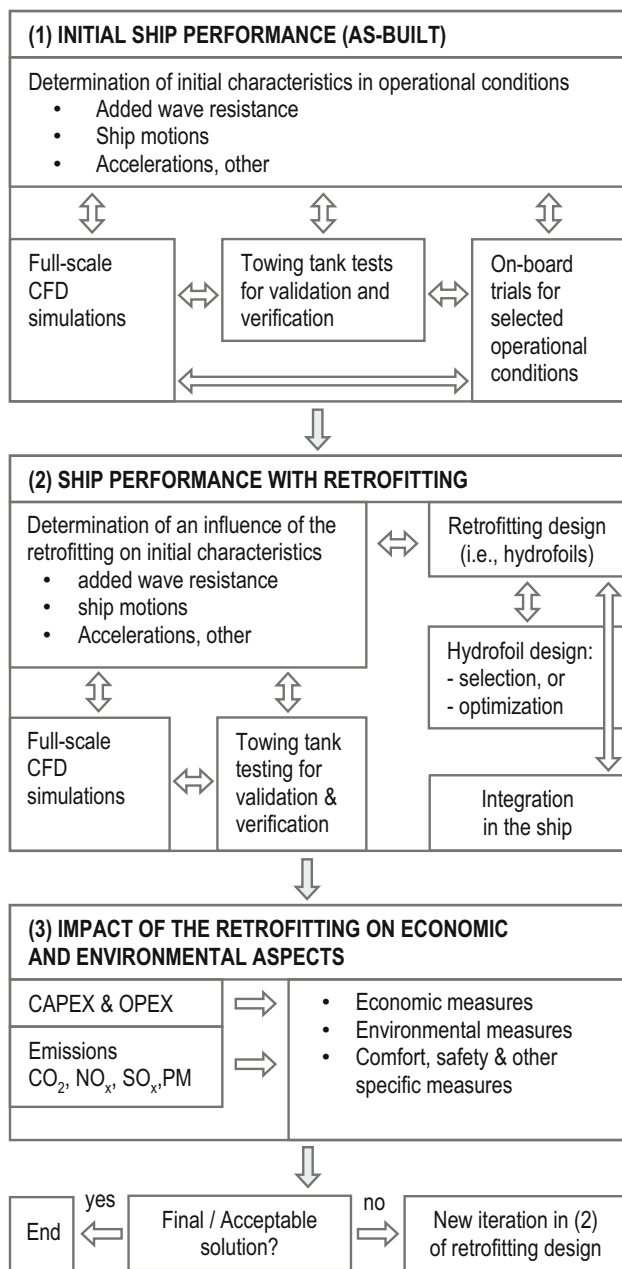
(1) INITIAL SHIP PERFORMANCE (AS-BUILT)

Determination of initial characteristics in operational conditions
- Added wave resistance
- Ship motions
- Accelerations, other

| Full-scale CFD simulations | Towing tank tests for validation and verification | On-board trials for selected operational conditions |

(2) SHIP PERFORMANCE WITH RETROFITTING

Determination of an influence of the retrofitting on initial characteristics
- added wave resistance
- ship motions
- Accelerations, other

Retrofitting design (i.e., hydrofoils)

Hydrofoil design:
- selection, or
- optimization

| Full-scale CFD simulations | Towing tank testing for validation & verification | Integration in the ship |

(3) IMPACT OF THE RETROFITTING ON ECONOMIC AND ENVIRONMENTAL ASPECTS

| CAPEX & OPEX | ⇒ | • Economic measures |
| Emissions CO_2, NO_x, SO_x, PM | ⇒ | • Environmental measures
• Comfort, safety & other specific measures |

End ⇐ yes — Final / Acceptable solution? — no ⇒ New iteration in (2) of retrofitting design

Fig. 33 Procedure for hydrofoil assessment in the retrofitting of existing ships

on hull motions and added wave resistance. The procedure has been tested on the case study ship and confirmed the indication of favourable operating conditions.

Declarations

References

Ahmed TM, Welaya Y, Abdulmotaleb SM (2017) Numerical modeling of the hydrodynamic performance of hydrofoils for auxiliary propulsion of ships in regular head-waves. In: Proceedings of the ASME 2017 36th international conference on ocean, offshore and arctic engineering, Trondheim. https://doi.org/10.1115/omae2017-61333

Aktas B, Turkmen S, Sasaki N, Atlar M (2016a) A study on hydrofoil application to assist wind farm support activity of a catamaran. In: 10th symposium on high-performance marine vehicles. https://www.researchgate.net/publication/315809739

Belibassakis KA, Filippas ES (2015) Ship propulsion in waves by actively controlled flapping foils. Appl Ocean Res 52:1–11. https://doi.org/10.1016/j.apor.2015.04.009

Belibassakis KA, Politis GK (2013) Hydrodynamic performance of flapping wings for augmenting ship propulsion in waves. Ocean Eng 72:227–240. https://doi.org/10.1016/j.oceaneng.2013.06.028

Berg A (1985) Trials with passive foil propulsion on M/S Kystfangst. Trondheim. Techn. Rep. Project (672.138)

Bøckmann E, Steen S (2013) The effect of a fixed foil on ship propulsion and motions. In: Third international symposium on marine propulsors Smp'13, (May), pp 553–561

Bøckmann E, Steen S (2016) Model test and simulation of a ship with wavefoils. Appl Ocean Res 57:8–18. https://doi.org/10.1016/j.apor.2016.02.002

Bøckmann E, Yrke A, Steen S (2018) Fuel savings for a general cargo ship employing retractable bow foils. Appl Ocean Res 76:1–10. https://doi.org/10.1016/j.apor.2018.03.015

Bowker J (2018). Coupled dynamics of a flapping foil wave powered vessel. University of Southampton, Doctoral Thesis

Bowker JA, Townsend NC, Tan M, Shenoi RA (2015) Experimental study of a wave energy scavenging system onboard autonomous surface vessels (ASVs). In: MTS/IEEE OCEANS 2015—Genova: discovering sustainable ocean energy for a new world. https://doi.org/10.1109/OCEANS-Genova.2015.7271484

Chiu F-C, Huang S-W, Wu T-L, Gou J-H, Tsai J-F (2018) Ship propulsion in irregular waves augumented by an active pitch oscillating bow fin. In: Proceedings of 8th PAAMES and AMEC, Busan

Ferziger JH, Peric M (2002) Computational methods for fluid dynamics. Springer. http://servidor.demec.ufpr.br/CFD/bibliografia/

FerzigerPeric-ComputationalMethodsforFluidDynamics3rdEd-2002.pdf

Filippas ES, Belibassakis KA (2014) Hydrodynamic analysis of flapping-foil thrusters operating beneath the free surface and in waves. Eng Anal Bound Elem 41:47–59. https://doi.org/10.1016/j.enganabound.2014.01.008

Huang S, Jiao J, Chen C (2021) CFD prediction of ship seakeeping behavior in bi-directional cross wave compared with in uni-directional regular wave. Appl Ocean Res. https://doi.org/10.1016/j.apor.2020.102426

Jiang Y, Bai J, Liu S, Zong Z, Li P (2022) Experimental investigation of T-foil hybrid control strategy for ship motion reduction in head seas. Ocean Eng. https://doi.org/10.1016/j.oceaneng.2021.110251

Jiao J, Sun S, Li J, Adenya CA, Ren H, Chen C, Wang D (2018) A comprehensive study on the seakeeping performance of high speed hybrid ships by 2.5D theoretical calculation and different scaled model experiments. Ocean Eng 160(June 2017):197–223. https://doi.org/10.1016/j.oceaneng.2018.04.051

Li F, Yu P, Wang Q, Li G, Wu X (2021) Numerical analysis of the effect of flexibility on the propulsive performance of a heaving hydrofoil undergoing sinusoidal and non-sinusoidal motions. Polish Marit Res 28(4):4–19. https://doi.org/10.2478/pomr-2021-0045

Moreira D, Mathias N, Morais T (2020) Dual flapping foil system for propulsion and harnessing wave energy: a 2D parametric study for unaligned foil configurations. Ocean Eng. https://doi.org/10.1016/j.oceaneng.2020.107875

Niklas K, Karczewski A (2020) Determination of seakeeping performance for a case study vessel by the strip theory method. Pol Maritime Res 27(4):4–16. https://doi.org/10.2478/pomr-2020-0061

Niklas K, Pruszko H (2019a) Full-scale CFD simulations for the determination of ship resistance as a rational, alternative method to towing tank experiments. Ocean Eng. https://doi.org/10.1016/j.oceaneng.2019.106435

Niklas K, Pruszko H (2019b) Full scale CFD seakeeping simulations for case study ship redesigned from V-shaped bulbous bow to X-bow hull form. Appl Ocean Res 89:188–201. https://doi.org/10.1016/j.apor.2019.05.011

Perić R, Abdel-Maksoud M (2018) Analytical prediction of reflection coefficients for wave absorbing layers in flow simulations of regular free-surface waves. Ocean Eng 147:132–147. https://doi.org/10.1016/j.oceaneng.2017.10.009

Politis G, Politis K (2014) Biomimetic propulsion under random heaving conditions, using active pitch control. J Fluids Struct 47:139–149. https://doi.org/10.1016/j.jfluidstructs.2012.05.004

Sheng-Wei H, Tsung-Lin W, Yu-Ting H, Jen-Hwa G, Jing-Fa T, Forng-Chen C (2016b) Effective energy-saving device of eco-ship by using wave propulsion. IEEE, pp 566–570. https://tethys.pnnl.gov/sites/default/files/publications/huang-et-al-20.pdf

Simonsen CD, Otzen JF, Joncquez S, Stern F (2013) EFD and CFD for KCS heaving and pitching in regular head waves. J Mar Sci Technol 18(4):435–459. https://doi.org/10.1007/s00773-013-0219-0

Stark C, Xu Y, Zhang M, Yuan Z, Tao L, Shi W (2022) Study on applicability of energy-saving devices to hydrogen fuel cell-powered ships. J Mar Sci Eng. https://doi.org/10.3390/jmse10030388

Suastika K, Silaen A, Aliffrananda MHN, Hermawan YA (2021) Seakeeping analysis of a hydrofoil supported watercraft (Hysuwac): a case study. CFD Lett 13(5):10–27. https://doi.org/10.37934/cfdl.13.5.1027

Terao Y, Isshiki H (1991) Wave devouring propulsion sea trial. In: Eighteenth symposium on naval hydrodynamics, pp 287–296

Tezdogan T, Demirel YK, Kellett P, Khorasanchi M, Incecik A, Turan O (2015) Full-scale unsteady RANS CFD simulations of ship behaviour and performance in head seas due to slow steaming. Ocean Eng 97:186–206. https://doi.org/10.1016/j.oceaneng.2015.01.011

Wang HD, Qian P, Liang XF, Yi H (2016) Vertical plane motion control of an S-SWATH vehicle with flapping foil stabilisers sailing in waves. Ocean Eng 121:184–195. https://doi.org/10.1016/j.oceaneng.2016.05.004

Wang D, Liu K, Huo P, Qiu S, Ye J, Liang F (2019) Motions of an unmanned catamaran ship with fixed tandem hydrofoils in regular head waves. J Mar Sci Technol (Japan) 24(3):705–719. https://doi.org/10.1007/s00773-018-0583-x

Wang X, Liu L, Zhang Z, Feng D (2020) Numerical study of the stern flap effect on catamaran' seakeeping characteristic in regular head waves. Ocean Eng. https://doi.org/10.1016/j.oceaneng.2020.107172

Wang WQ, Li W, Yan Y, Zhang J (2022) Parametric study on the propulsion and energy harvesting performance of a pitching foil hanging under a wave glider. Renew Energy 184:830–844. https://doi.org/10.1016/j.renene.2021.11.109

Xu GD, Duan WY, Zhou BZ (2017) Propulsion of an active flapping foil in heading waves of deep water. Eng Anal Bound Elem 84(July):63–76. https://doi.org/10.1016/j.enganabound.2017.08.014

Yasukawa H, Ishikawa T (2017) Improvement of propulsive performance of a catamaran in waves by a biologically inspired hydrofoil. In: 11th symposium on high-performance marine vehicles. Zevenwacht

Zhang Y, Xu L, Zhou Y (2022) A wave foil with passive angle of attack adjustment for wave energy extraction for ships. Ocean Eng. https://doi.org/10.1016/j.oceaneng.2022.110627